Oil & Natural Gas Technology

DOE Award No.: DE-FC26-06NT43067

Creation of Sediment Models
(Task 3 Technical Report)

Mechanisms Leading to Co-Existence of Gas and Hydrate in Ocean Sediments

Submitted by:
The University of Texas at Austin
1 University Station C0300
Austin, TX 78712-0228

April 17, 2007

Office of Fossil Energy

MECHANISMS LEADING TO CO-EXISTENCE OF GAS AND HYDRATE IN
OCEAN SEDIMENTS

CONTRACT NO. DE-FC26-06NT43067

Deliverable 3:
Report on Results of Task 3 "Creation of Sediment Models"

Prepared by

Steven L. Bryant
Department of Petroleum and Geosystems Engineering
The University of Texas at Austin
1 University Station   C0300
Austin, TX   78712-0228
Phone: (512) 471 3250
Email: steven_bryant@mail.utexas.edu

Ruben Juanes
Department of Civil and Environmental Engineering
Massachusetts Institute of Technology
77 Massachusetts Avenue, Room 48-319
Cambridge, MA 02139
Phone: (617)253-7191
Email: juanes@mit.edu

Prepared for
U.S. Department of Energy - NETL
3610 Collins Ferry Road
P.O. Box 880
Morgantown, WV 26508

Objective of Task 3

In this task a set of model sediments (dense random packings of spheres with several size distributions) was created. We considered several codes for use in this study including PFC2D/3D (commercial software), S3D (commercial software) and research codes developed at UT-Austin (Thane, 2006). We elected to use PFC2D/3D at MIT and the Thane codes at UT-Austin, as these computer codes have been validated in previous research.

The sediment models developed at UT were generated using a cooperative rearrangement algorithm, and they have periodic boundaries to eliminate edge effects. For all packings the spatial locations of spheres and the packing porosity were recorded. Pore throats were identified in these models with Delaunay tessellation. A network structure that preserves the topology of the throats was extracted. The topology and geometry of the network representation of pore space were recorded for each packing. On the other hand, the PFC models were generated with boundary and initial conditions, including gravity, that simulate relevant depositional environments.

The packings will serve as the foundation for studying at the grain scale the competition between capillarity-controlled displacements (of brine by gas, and of gas by brine), formation of hydrate (at the brine/gas interface), and fracturing (induced by pore pressure in the gas phase).

Summary of Findings in Task 3

Several dozen model sediments – dense, random packings of spheres with several grain size distributions – were constructed with two different algorithms. The geometry of the model sediments has been characterized (spatial coordinates of spheres, void fraction, grain radial distribution functions, pore throat size distributions, pore space topology). The algorithms yield packings with similar and consistent properties.

The model sediments are good representations of the hydrate-bearing strata in locations such as the Mackenzie Delta in Canada. On the other hand the models have smaller porosities, in the range of 30% to 40%, than many ocean sediments containing hydrates, which exhibit void fractions of 50% to 80%. The fact that a wide range of porosities are encountered in gas hydrate provinces is important, but accounting for the full range is not the primary goal of this project. Rather, we seek a fundamental understanding of the competition and coupling between capillarity control and fracture mechanics control of the movement of methane gas into brine-saturated sediments. Moreover, such high values of porosity in clayey sediments likely include a very high fraction of microporosity (filled with chemically-bound water) that remains inaccessible to methane gas and hydrate.

Densely packed model sediments like those constructed in this Task permit the fastest development of this understanding. The methods we are using to study the capillarity/mechanics coupling are not "hard wired" to those models, so extending the methods to low density sediments will be feasible.

Summary of Some Ocean Sediment Characteristics

In this section we report on some characteristics and mechanical properties of hydrate-bearing ocean sediments. The section is organized by geographic location: Hydrate Ridge (offshore Oregon), Blake Ridge (offshore South Carolina), and the Gulf of Mexico.

Southern Hydrate Ridge, Oregon

Grain-Size

The ODP Leg 204 determined that sediments in the summit, east flank and west flank of the ridge have small fluctuations in grain-size distribution, see Figures 1, 2 and 3 (Gracia et al., 2006). Their average mean size is 8.4ϕ, equivalent to $2^{-8.4}$ mm or 3 micrometers. The bulk mineralogy is dominated by clays (30%-60%), quartz (25%-40%), feldspars (10%-25%), and calcite (<5%).
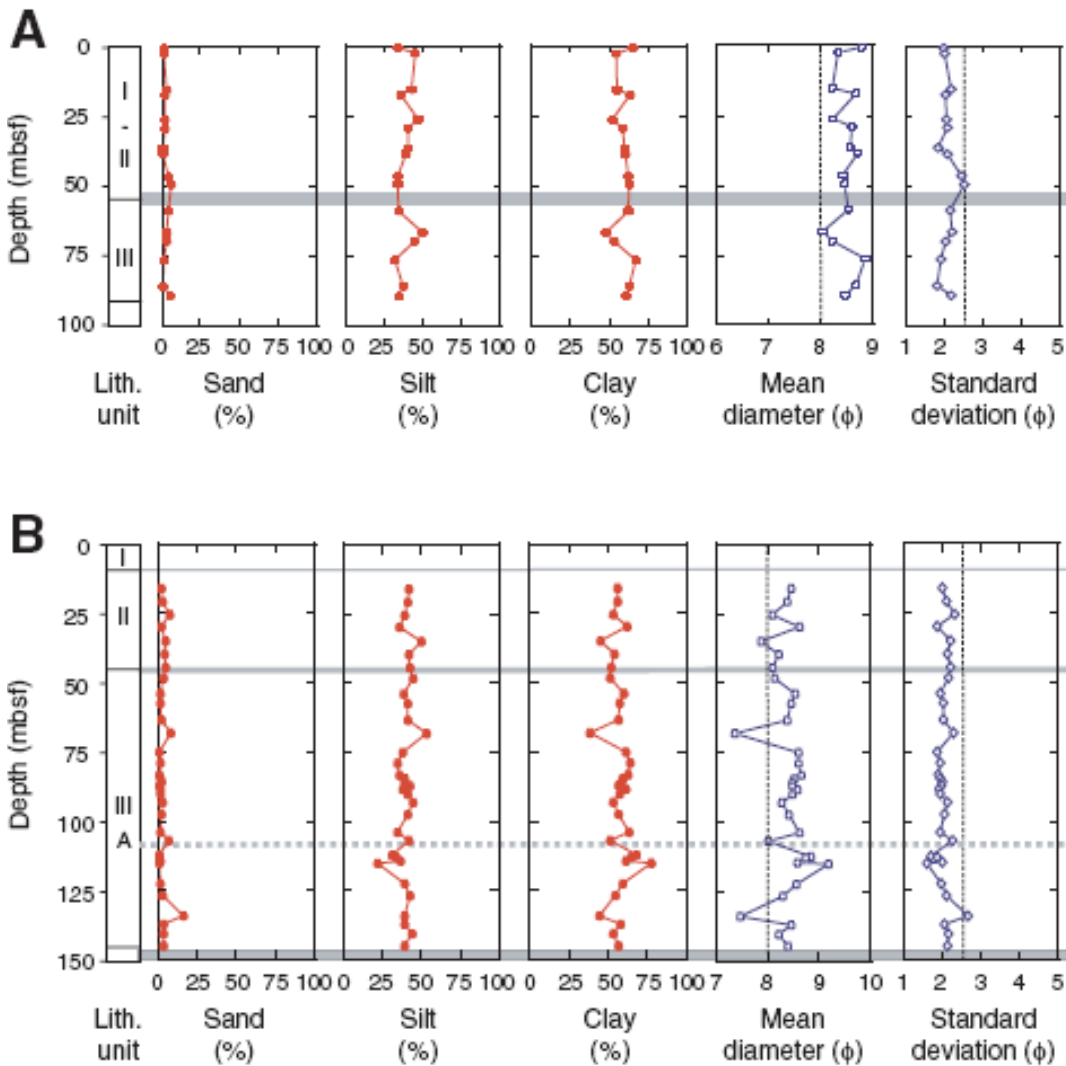

Figure 1. Downhole variations of grain size and textural statistical parameters from (A) Hole 1249C and (B) Hole 1250C located at the summit of southern Hydrate Ridge. (Gracia et al., 2006).
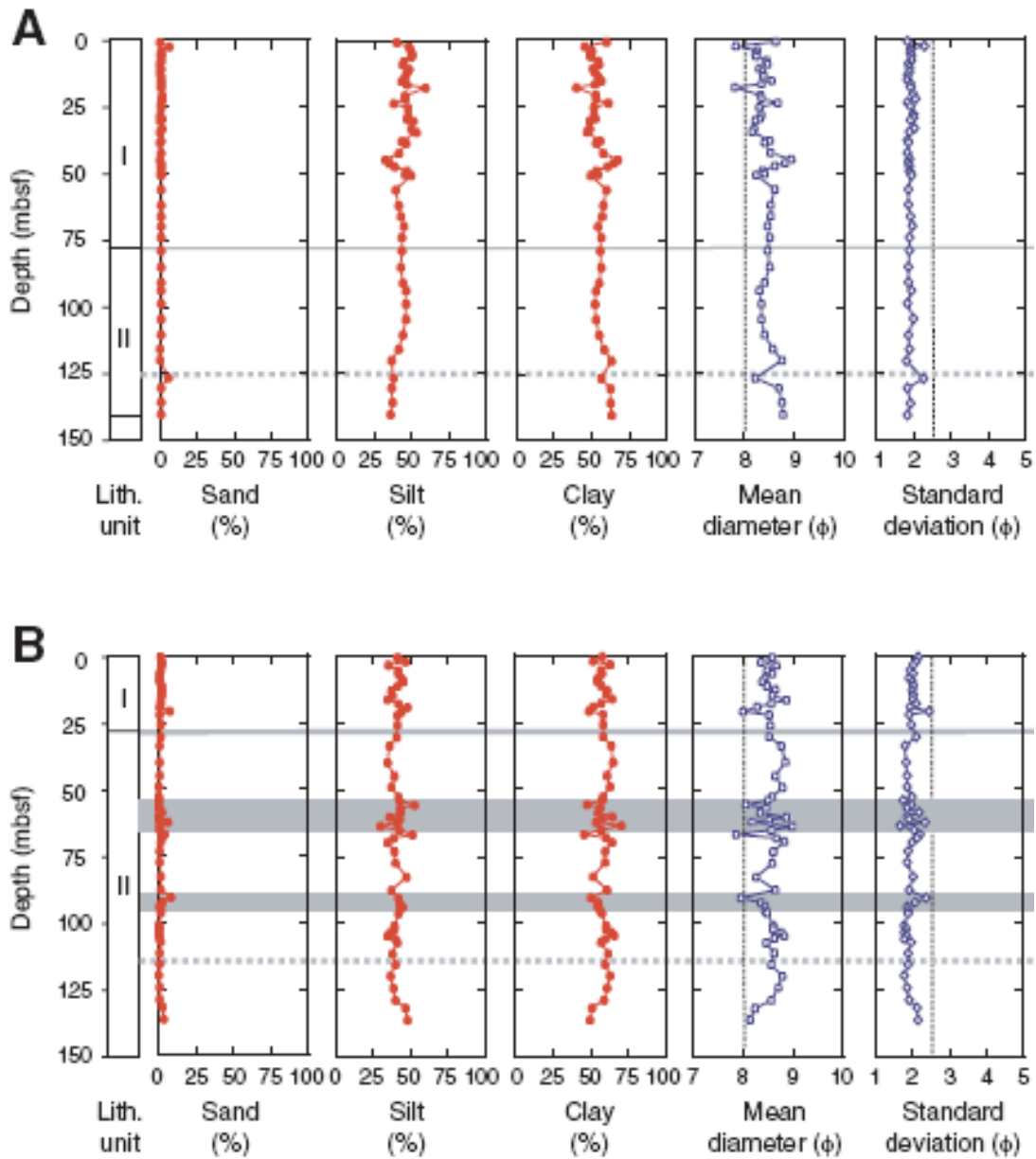
Figure 2. Downhole variations of grain size and textural statistical parameters from (A) Hole 1244E and (B) Hole 1246B located on the east flank of southern Hydrate Ridge. (Gracia et al., 2006).
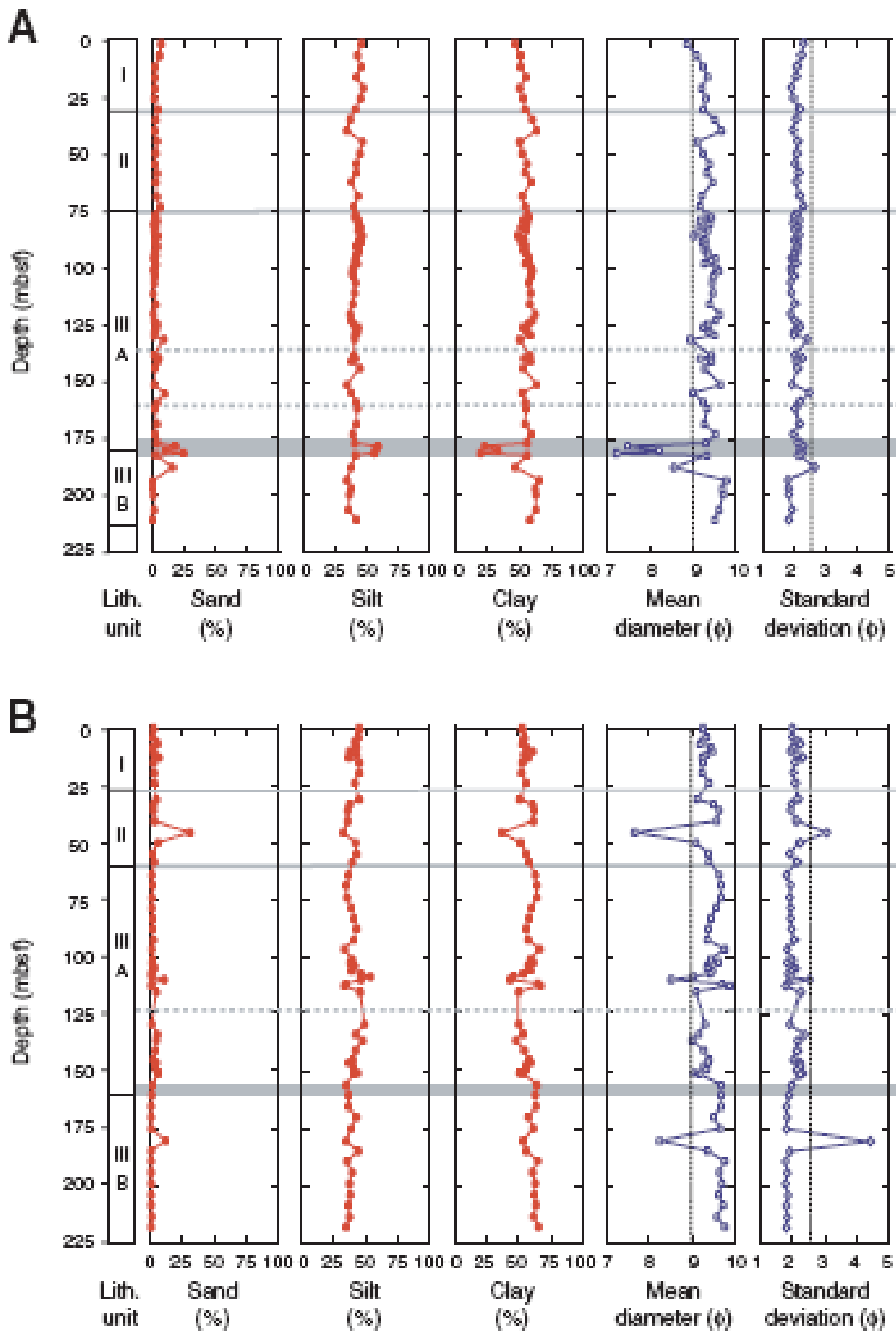
4

Figure 3. Downhole variations of grain size and textural statistical parameters from (A) Hole 1245B and (B) Hole 1247B located on the east flank of southern Hydrate Ridge. (Gracia et al., 2006).

Porosity

Sediment porosities appear to be highest at Sites 1251 and 1252 in the slope basin, with values of ~75% in the upper 5 m below seafloor (Riedel et al., 2006). Porosity is generally lower by about 10 percentage points at all other sites (Figure 4). Sediment density varies between 1.4 and 1.8 g/cm^3.
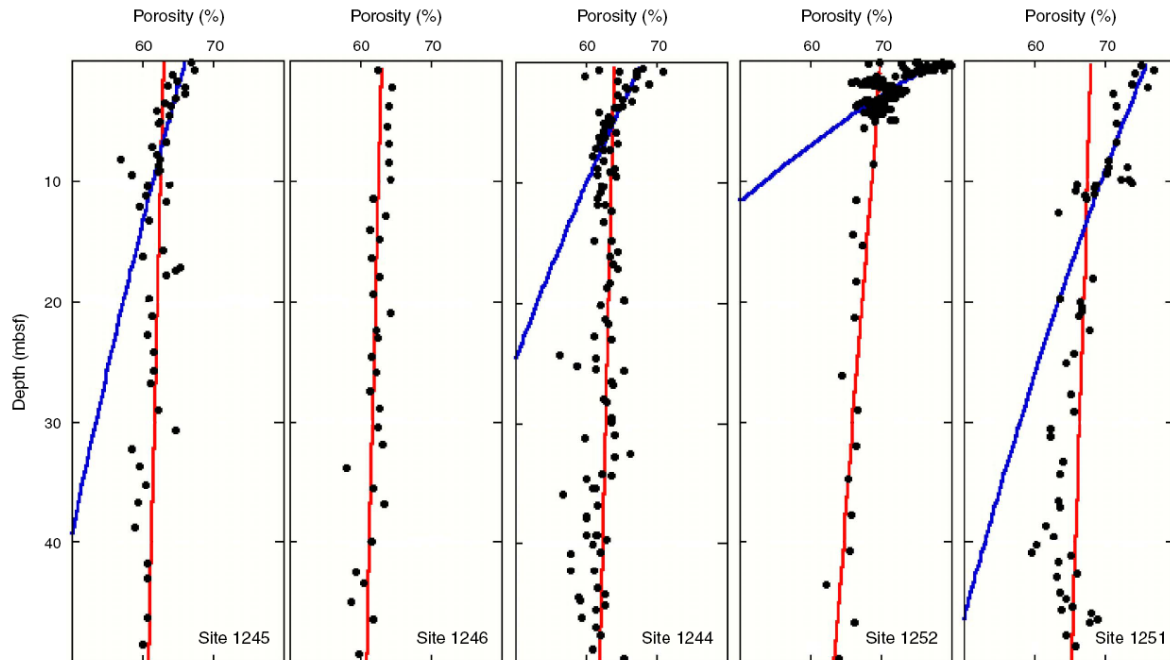

Figure 4. Downcore porosity (solid circles) for the upper 50 mbsf at Sites 1244, 1245, 1246, 1251, and 1252. The red line is a best-fit using Athy's law for the entire cored section. The blue line is a best-fit using Athy's law for the upper 10 mbsf. (Riedel et al., 2006).

Hydraulic Conductivity

Eight cores were taken at 5 to 136 mbsf. Seven of the eight were from the hydrate stability zone and the eighth was from the free gas zone. In situ hydraulic conductivity varies between 1.5×10^{-7} and 3×10^{-8} cm/s and shows no trend with depth (Tan et al., 2006).

Strength Testing

Drained and undrained strength testing on eight whole-core samples recovered from drilling at Hydrate Ridge, Cascadia Continental Margin, were performed in the laboratory (Tan et al., 2006). During the drained Constant Rate of Strain Test, the applied effective stress ranges from 5 kPa to 40 kPa. Then, while maintaining the same effective stress, the axial stress and cell pressure are increased in increments of 100 kPa until the cell pressure reaches 400 kPa. For the eight cores, at failure, the axial strain ranges from 0.2% to 0.5%, while the maximum vertical stress ranges from about 18 kPa to 30 kPa and maximum effective vertical stress ranges from 16 kPa to 25 kPa.

During undrained triaxial testing, the applied effective stress ranges from 10 kPa to 20 kPa. Then, while maintaining the same effective stress, the axial stress and cell pressure are increased by an increment of 50 kPa. For the eight core samples, at failure, the axial strain ranges from 10% to 20% and the maximum vertical effective stress ranges from 0.1 MPa to 2.0 MPa (Figure 5).
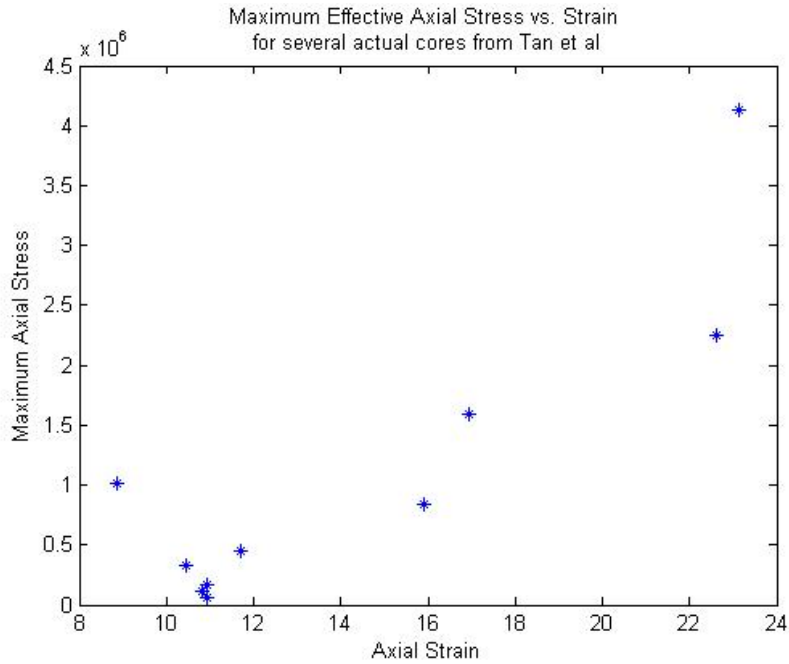

Figure 5. Failure points during triaxial compression tests for samples recovered from drilling at Hydrate Ridge, analyzed by Tan et al. (2006).

Blake Ridge, South Carolina

Grain-size Distribution

Clays and quartz with grain-sizes on the order of microns dominate. In the vertical profile, decreases in chlorinity coincide with spikes in coarse-grained sediments (Figure 6).

Porosity

At ODP Site 997, core porosity declines rapidly in the first 100 mbsf (80% – 65%) and slowly from 100 to 600 mbsf (65% – 47%). The decrease in the rate of porosity decline with depth beneath 100 mbsf is interpreted to record underconsolidation and overpressure (Flemings et al., 2003).
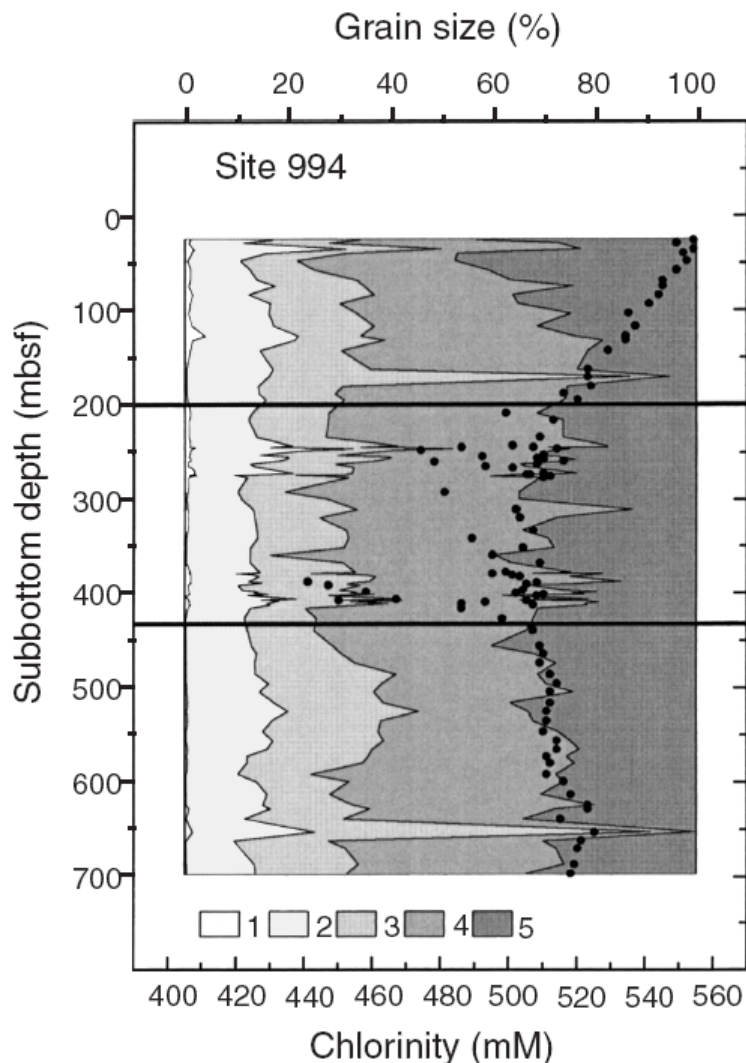

Figure 6. Sediment grain-size distribution (lines) and pore-water chlorinity (solid circles; after Paull, et al., (1996)) in the column at ODP Site 994. Grain-size fractions in millimeters: 1 = >0.05; 2 = 0.05-0.01; 3 = 0.01-0.005; 4 = 0.005 - 0.001; 5 = <0.001. Bold lines limit the gas hydrate zone (Ginsburg et al., 2000).

Gulf of Mexico

Grain-Size Distribution

Clays and silty clays dominate in the three core samples of the uppermost 5 mbsf. More than 48% of the sediment is of clay size (<2 micrometers) at each site, while less than 5% of the sediment is within the sand range (>75 micrometers), see Figure 7 (Francisca et al., 2005).
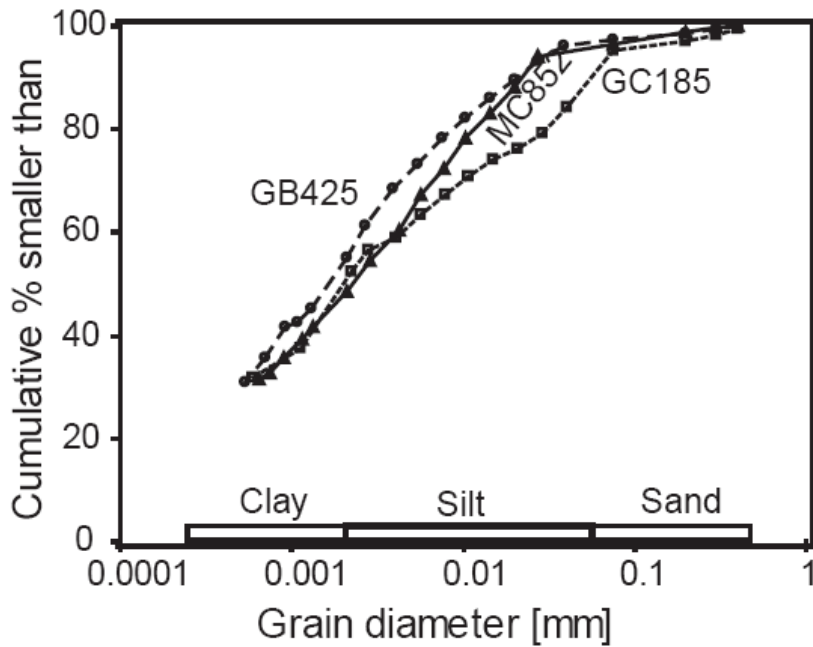
Figure 7. Grain size distribution for cores at sites GB425, MC852, GC185. (Francisca et al., 2005).

Methods for Building Model Sediments

In this section we give an overview of the methods used to create the model sediments and we describe the main properties of interest of the models.

Cooperative rearrangement

This algorithm is one of simplest yet most effective ways to produce dense random packings. The key idea is that density is increased by adding small increments to the radius of spheres within a domain. The increment causes some neighboring spheres to overlap. Physical consistency is maintained by moving the spheres apart until overlap is removed. The steps for producing a monodisperse packing are as follows:

1. create n Poisson points (i.e. x, y, z coordinates chosen at random) within a unit cell;
2. define a sphere centered at each Poisson point and set its diameter D to a small value;
3. loop through the list of spheres:
     a. for each sphere, loop through all the other spheres:
          i. compute distance s between centers of test sphere and other sphere;
          ii. if $s < D + \delta$, where δ is a user-specified tolerance, then the spheres overlap; move the neighbor sphere away from the test sphere so that they are in point contact;
4. repeat (3) until no overlap exceeds δ;
5. compute the porosity of the packing;
6. if the change in porosity from previous iteration is small enough (less than 0.01 %), stop; otherwise, increment the diameter of each sphere by ΔD and go to (3)

This algorithm is readily generalized to a unit cell with periodic boundaries. It has also been extended to create a distribution of sphere sizes (Thane, 2006). All packings in this project have periodic boundaries. That is, the spheres near any face of the unit cell are in virtual contact with spheres near the opposite face. This eliminates edge effects from the packings. This is an important consideration, since any smooth confining surface, such as the wall of a box, will impose local order on the packing. Such a deviation from randomness would reduce the physical representativeness of the packing.

Periodic boundaries also enable us to create arbitrarily large domains simply by replicating the unit cell. In this fashion we can circumvent some problems associated with finite size effects. The size of the unit cell is typically larger than the correlation length in the radial distribution function. Thus the fact that a repeating unit cell is used to construct the larger packing does not introduce noticeable artifacts.

Discrete Element Modeling (DEM)

Overview of Discrete Element Modeling

The Discrete Element Method (DEM) (Cundall and Strack, 1979) has proved a valuable tool to study the mechanisms for deformation and failure of granular materials with variable degree of cementation (Bruno and Nelson, 1991). Moreover, based on simple geometric arguments, stress variations (and subsequent deformation) have been shown to affect flow properties such as porosity and permeability (Bruno, 1994).

In DEM, each element or grain is identified separately by its own mass, moment of inertia and contact properties. For each grain, its translational and rotational movements are described by solving Newton's second law of motion. The mechanical behavior at the deformation region of grain contact is approximated by introducing a grain contact model, such as a system of a spring, dashpot and slider. The movement of a grain is dictated by the net force and moment acting on it. For a dry model, that is, one in which pore pressures are negligible, the forces for each grain may include: (1) contact force F_c due to the deformation at the grain contacts, (2) damping forces F_d due to grain non-elastic collisions; (3) external forces F_b due to gravity and prescribed tractions at the boundaries. The contact force F_c can be further split into normal and tangential components, F_c^n and F_c^t, respectively. Bulk behavior of a granular system is determined by all individual grain–grain interactions. For the analysis of dry samples, that is, systems in which the pore pressure is negligible, the interactions between particles can be associated with a network of grain–grain contact forces that connects the centroids of grains that are in contact (Figure 8).
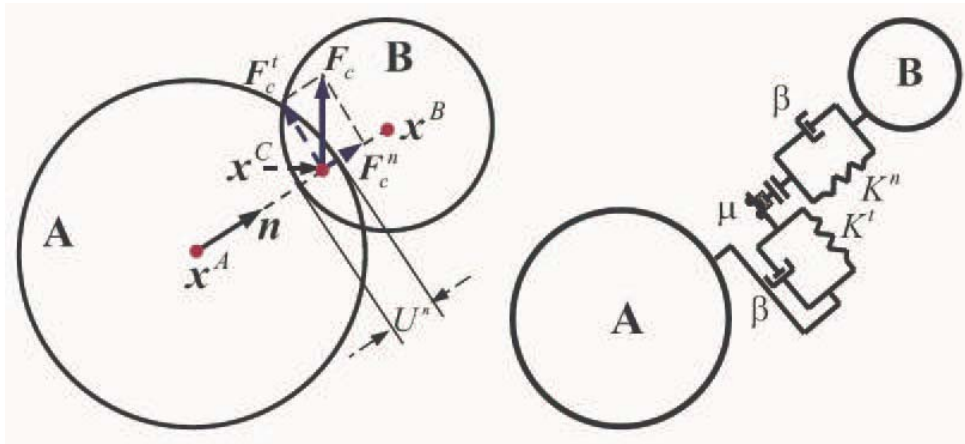

Figure 8. Schematic diagram of a grain–grain contact (left) and the associated contact model in a Discrete Element Model (right) (Jin, 2006).

The motion of an individual grain in the multi-grain system is determined by the resultant force F and moment M acting upon it. The grain motion can be described by the following equations of motion:

$$m x'' = F ; \qquad I \theta'' = M.$$

11

Here, x and θ are the position vector of the grain centroid and the angle vector of rotation about the centroid, respectively; the double prime symbols denote second time derivatives of the position and rotation angle; and m and I are the mass and moment of inertia, respectively. The equations of motion must be solved simultaneously for all grains in the system via a numerical integration scheme. In DEM, explicit solution schemes with a single force evaluation per time step are preferred. A commercial DEM code, PFC2D/3D (ITASCA, 2005), has been used.

In PFC2D/3D each grain is treated as a sphere. At each timestep, the equations of motion are applied to each sphere to update its position and velocity. The timestep is sufficiently small so that only immediately neighboring particles exert forces. Energy is dissipated through frictional losses and mechanical damping forces. Particles can be bonded at a contact point or over a contact area, simulating cementation. Micromechanical parameters, such as particle stiffness and bond strength, are set iteratively so that the model sediment packings behave closely to actual sediments that have been collected in scientific drilling voyages and subjected to compression testing.

Generation of Model Sediments with PFC2D/3D

The sedimentation process is simulated by allowing particles in a walled box to fall and settle under gravitational acceleration (Figure 9 and Figure 10). We have used 2D packings to demonstrate the applicability of the approach. One feature of PFC2D that makes this possible is that we can use the contact mechanics between 3D spheres (rather than 2D cylinders) to describe the stress-strain relationship at the contact between two grains. The porosities of 2D packings are smaller than of 3D packings, but stress-strain behavior of the assembly is comparable. Balls and walls have normal stiffness and shear stiffness in units of force per displacement [N/m]. The side walls simulate soft and smooth confining material, so they have a significantly smaller normal stiffness than the balls, and they do not have any shear stiffness. The model operates under a frictional-slip condition. The friction for balls and walls is set to 0.5. When shear force exceeds the maximum shear force (0.5 × normal force), slip is allowed to occur, and shear force is kept constant at the maximum shear force.

300-ball and 1000-ball model sediments were generated with Gaussian grain size distributions. The mean grain size was set at 6 micrometers and standard deviation at 2 micrometers. The Cumulative Density Functions (CDF) of the radii for each sample are shown in Figure 11.
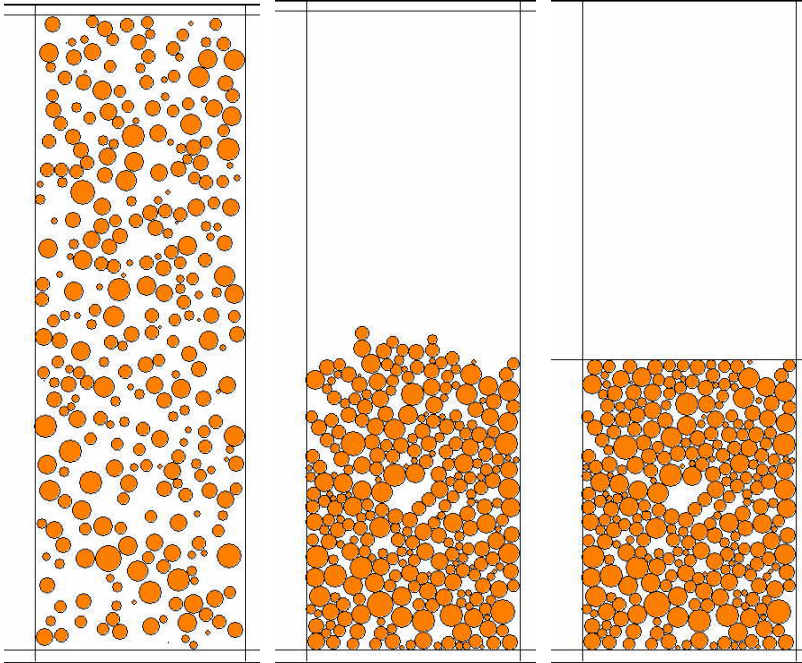
Figure 9. Simulated sedimentation of 300 balls. **Left:** Particles at generation. The particles, with a Gaussian grain size distribution similar to the field sample, are randomly placed between the four walls. **Center:** Model sediment after settling due to gravity. **Right:** Model sediment after compaction by the top wall.

Figure 10. Simulated sedimentation of 1000 balls. **Left:** Particles at generation. The particles, with a Gaussian grain size distribution similar to the field sample, are randomly placed between the four walls. **Center:** Model sediment after settling due to gravity. **Right:** Model sediment after compaction by the top wall.
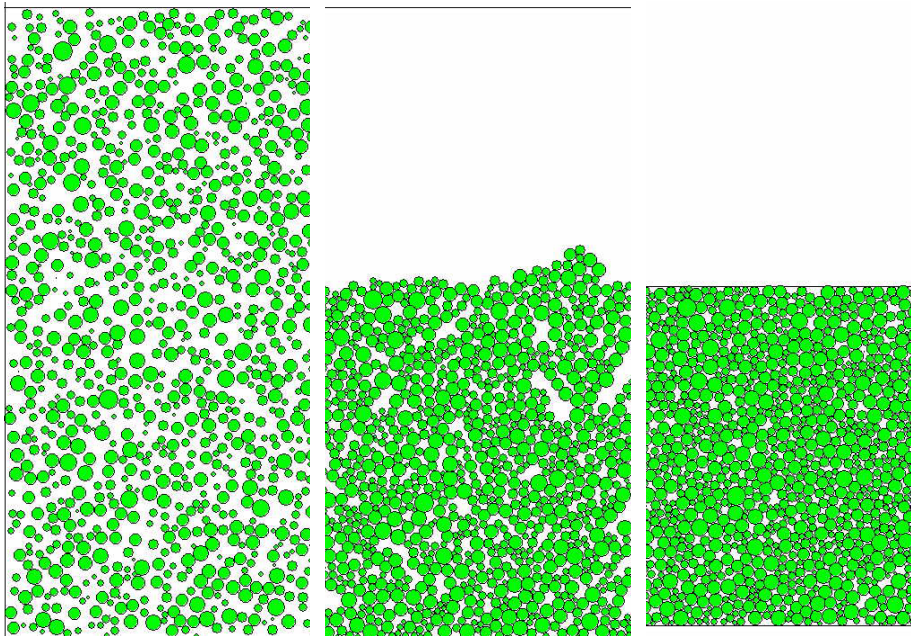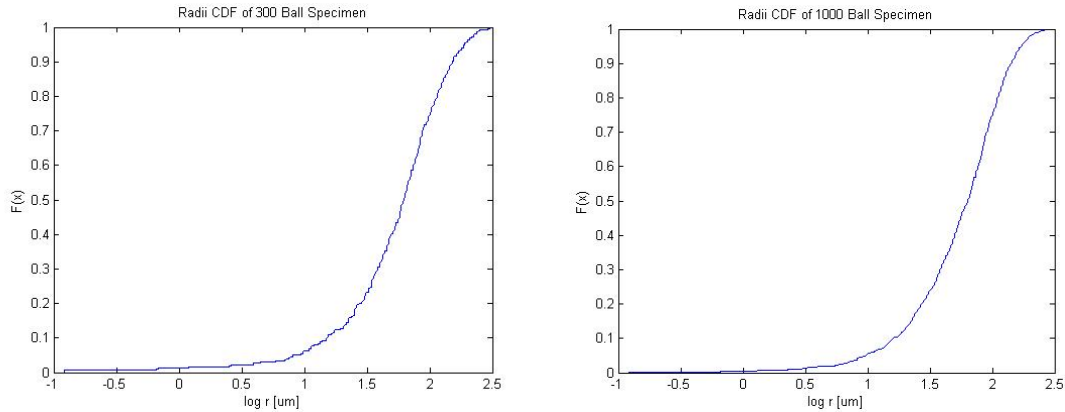
Figure 11. Cumulative Density Function of grain size distribution for 300-ball specimen (left) and 1000-ball specimen (right). F(x) is the cumulative fraction of balls smaller than the specified radius.

After the particles have settled on the bottom of the walled box, the sample is prepared for biaxial compression testing. The top wall is moved down to compact the top of the sample. Next, a constant confining stress is applied on the specimen equally by all four walls. Then, contact bonds or parallel bonds may be installed. Contact bonds act like glue. They keep particles together at their point of contact until their normal strength or shear strength is exceeded by contact forces. They do not prevent rotation. When contact bonds are activated, the frictional-slip is deactivated for bonded particles. Friction is then activated if the bonds break.

The sample may also be parallel bonded. Parallel bonds simulate cementation between particles. They have constant normal and shear stiffness, uniformly distributed over an area around the point of particle contact. When there is relative motion between the bonded particles, the bonds transmit a force and moment in resistance to that motion. The parallel bond stiffness acts in parallel to the ball stiffness. Parallel bonds have tensile normal bond strength and shear bond strength. If either the force or moment acting on two bonded particles exceeds the bond strength, the bond breaks.

Biaxial Testing with PFC

Once the preparation is complete, model sediments are subjected to triaxial loading at various confining pressures. The top and bottom walls apply compressive vertical stresses to the sample, while the vertical walls maintain a specified confining pressure. The stress-strain behavior of the model should closely match the actual sediment stress-strain behavior reported from laboratory tests under various experimental conditions.

We performed biaxial compression testing on specimens with 300 balls and 1000 balls. The side walls provided a constant confining pressure of 20 kPa, while the top and bottom walls were moved inwards at a constant strain rate. As the samples were compressed, the axial stress increased until specimen failure (Figure 12 and Figure 14). Four snapshots of the sample are shown over the course of the test (Figure 13 and Figure 15). The specimen porosity decreased throughout the test (Figure 16).

Figure 12. Axial stress vs. axial strain for specimen with 300 balls. Numbers with stars indicate the four points at which snapshots (Figure 13) are taken of the sample.

 Figure 13. Snapshots of specimen with 300 balls during biaxial compression testing. As the sample is compressed, it becomes shorter and wider. **Upper Left**: Beginning of test. **Upper Right**: Snapshot two. **Lower Left**: Snapshot three. **Lower Right**: Snapshot four.
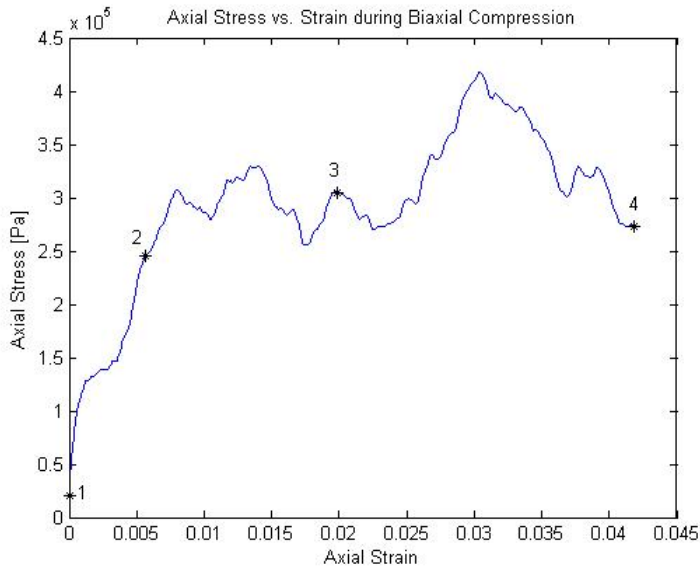
Figure 14. Axial stress vs. axial strain for specimen with 1000 balls. Numbers with stars indicate the four points at which snapshots (Figure 15) are taken of the sample.
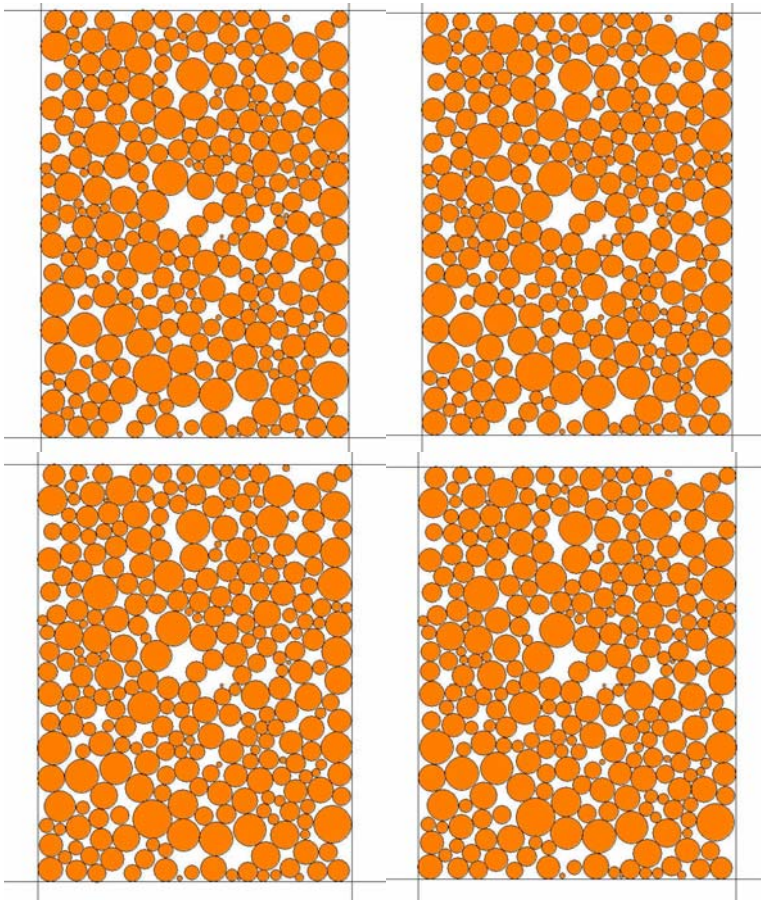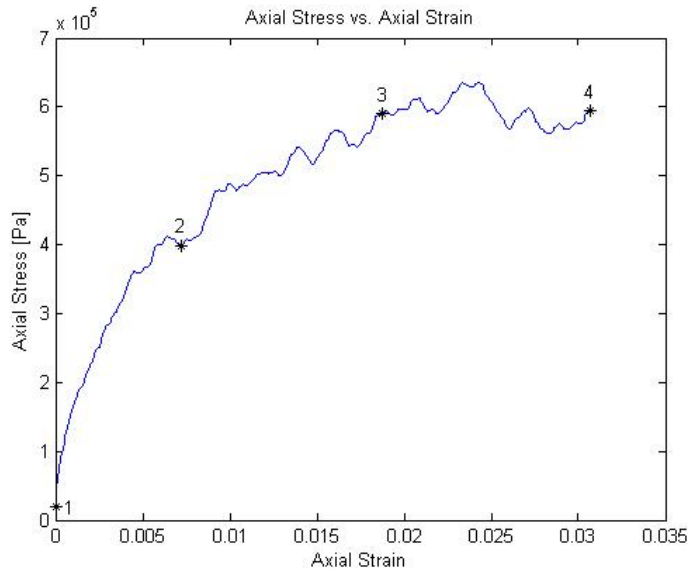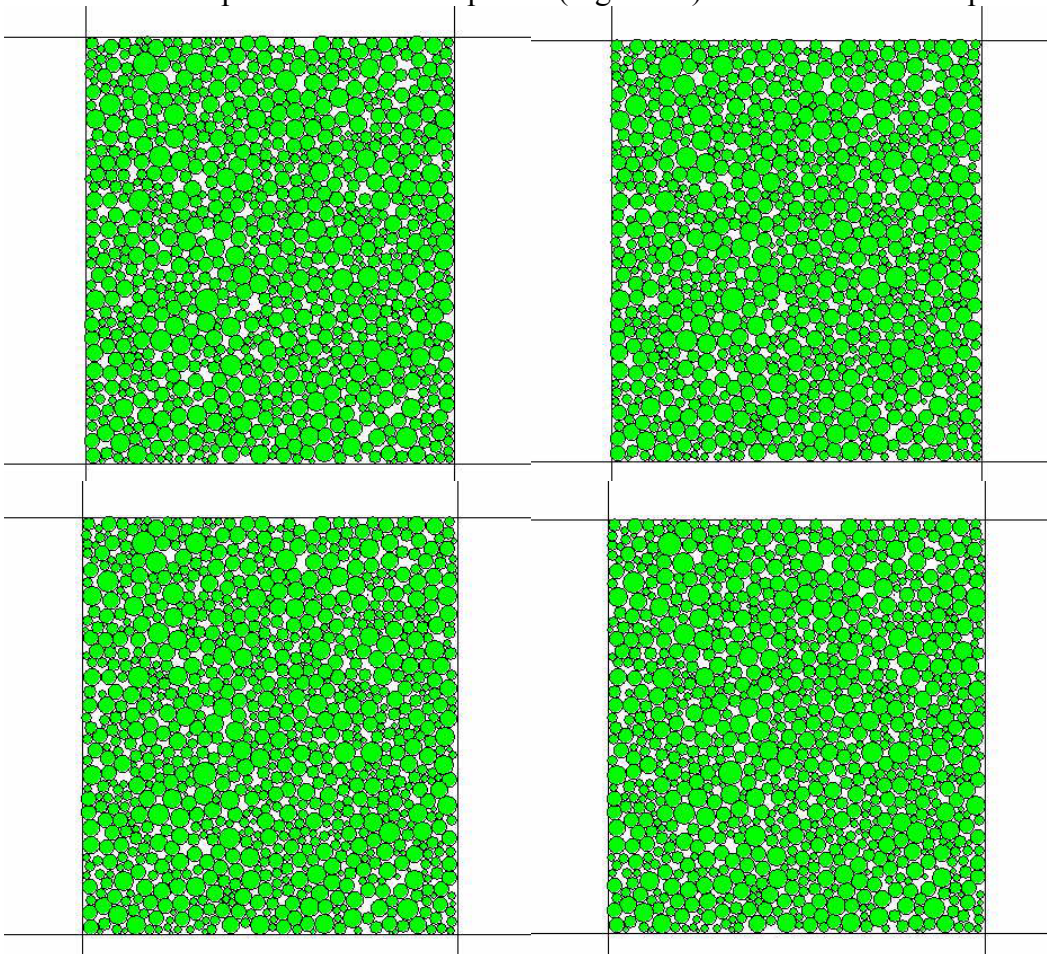

Figure 15. Snapshots of specimen with 1000 balls during biaxial compression testing. **Upper Left**: Beginning of test. **Upper Right**: Snapshot two. **Lower Left**: Snapshot three. **Lower Right**: Snapshot four.
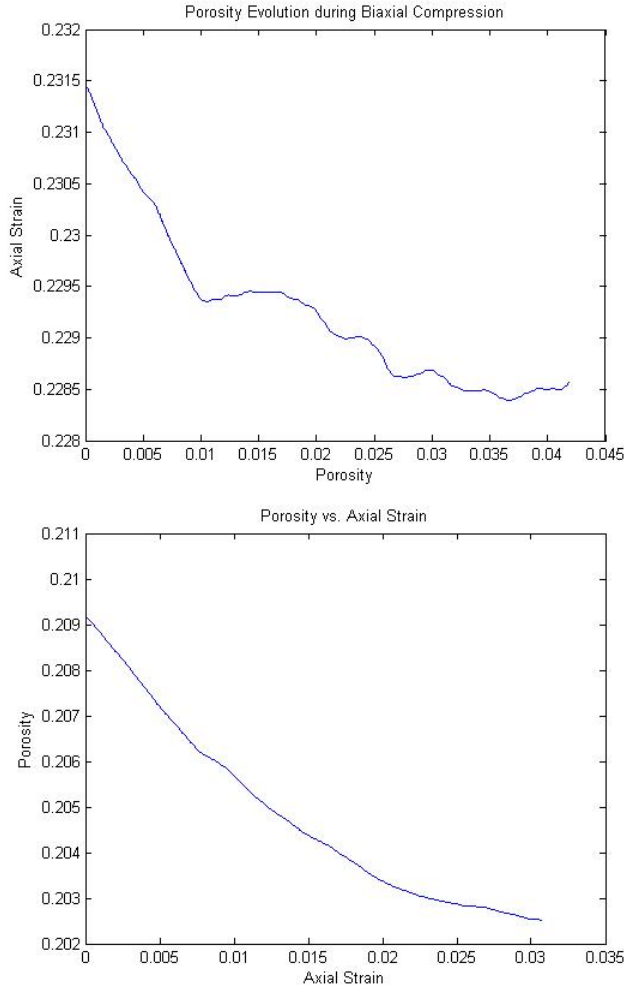
Figure 16. Porosity evolution with axial strain for 300 balls (top) and 1000 balls (bottom).

Effect of micromechanical parameters and testing conditions

Samples with greater particle stiffness fail at larger axial strains and stresses than samples with lower stiffness. Figure 17 shows the stress-strain curves for two 1000-ball samples subject to biaxial loading. The samples are geometrically identical initially, but with a difference in ball stiffness by a factor of three.

Figure 18 shows the stress-strain curve for the unbonded 1000-ball specimen, and two different confining pressures. As expected, the maximum stress at failure is increased and pronounced for the higher confining pressure.

Unbonded samples fail at lower strains and stresses than bonded samples. For the contact bonded sample (Figure 19), the material responds elastically during the initial strain stages, up until a strain of about 0.05. As the strain increases and bonds break, the material fails. The parallel bonded sample behaves elastically until a strain of about 0.004 (Figure 20).

17
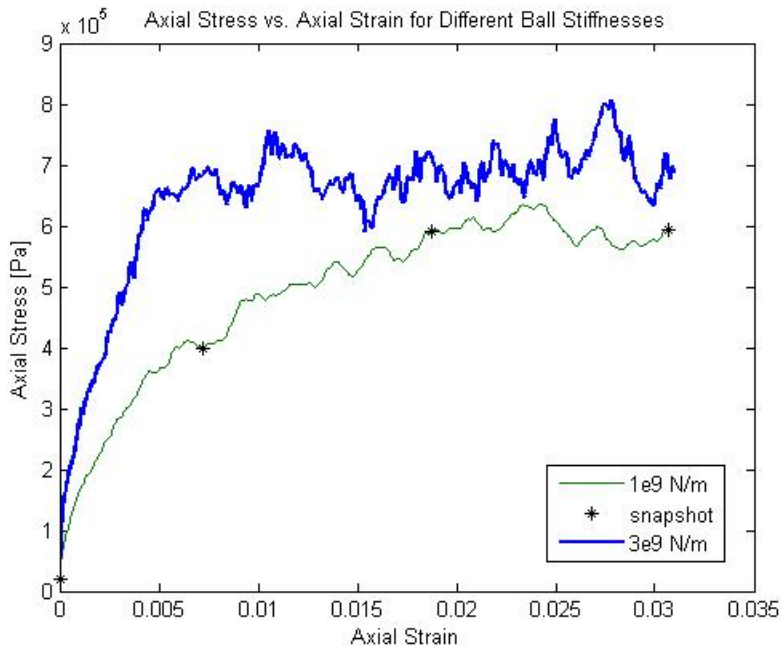
Figure 17. Axial Stress vs. Strain for unbonded 1000-ball specimen, with lateral confining pressures of 20 kPa and 1 MPa. The ball normal and shear stiffness is 10^9 Pa. The strain is carried out past failure to compare the magnitude of the two curves.
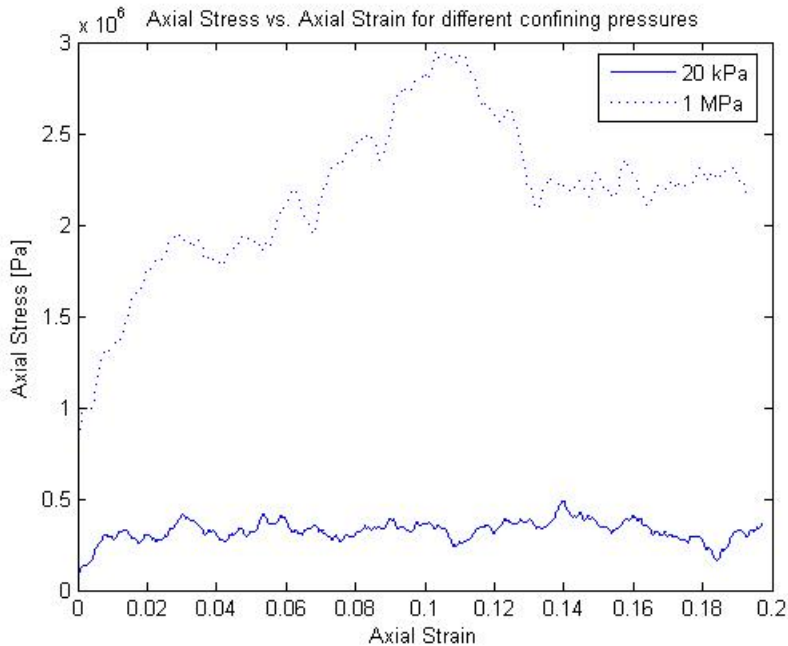
Figure 18. Axial Stress vs. Strain for unbonded 1000-ball specimen, with lateral confining pressures of 20 kPa and 1 MPa. The ball normal and shear stiffness is 10^9 Pa. The strain is carried out past failure to compare the magnitude of the two curves.
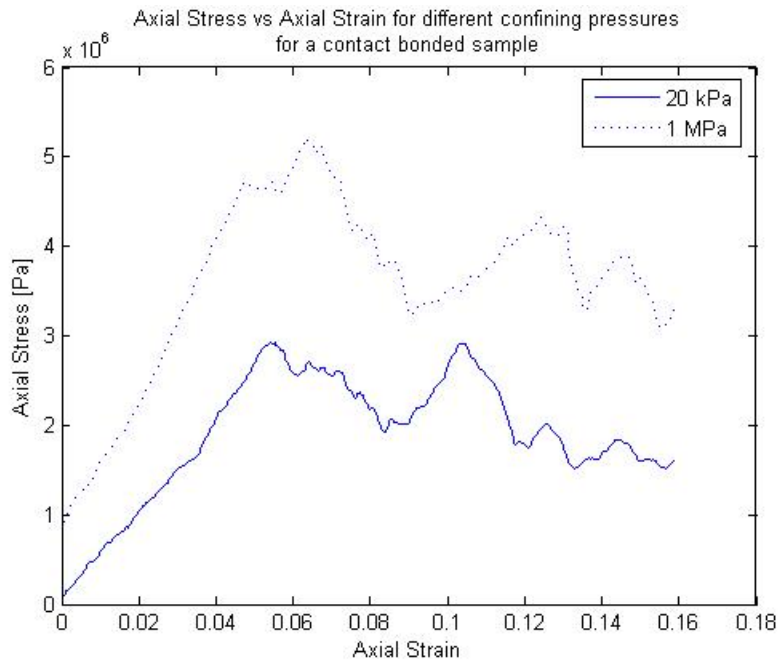
Figure 19. Axial stress vs. strain for 1000-ball contact bonded sample. The normal and shear bond strengths are set at 0.1 kN. The compression is continued past failure.
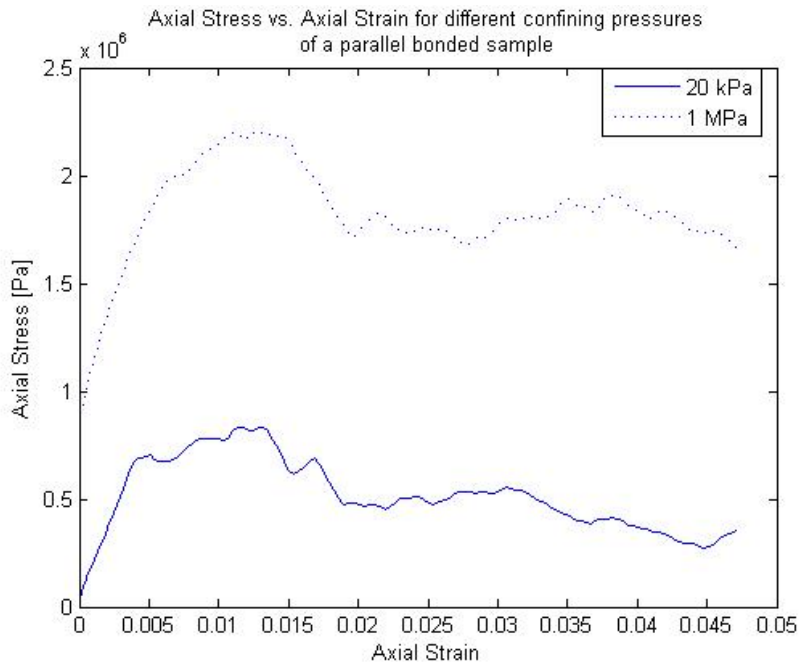
Figure 20. Axial stress vs. strain for 1000-ball parallel bonded sample. The normal and shear bond strengths are set at 4 MPa/m. The compression is continued past failure.

Discussion of the Model Sediments

We address the question of applicability of the models to different geologic settings and to various applications. Finally we provide a guide to the data files containing the model sediments. More details are in the Appendix.

Applicability of model sediments to hydrate-bearing formations

By design, both methods for building model sediments result in packings with several salient features:

- ❑ Random grain locations;
- ❑ Maximally dense packing;
- ❑ Load-bearing structure made up of grain-to-grain contacts;

These features are characteristic of coarse grained (>50 micron) formations containing hydrates, such as the Mackenzie Delta. Our model sediments are also encountered in laboratory experiments on hydrate formation, where bead packs and sand packs are routinely employed as surrogates for natural sediments.

**Random packing** is the single most important feature of real sediments that a grain scale model must capture. Ordered packings are conceptually and mathematically convenient but cannot be used for quantitative understanding of natural sediments. By random packing we mean that no crystalline structure (extensive regions of regular packing) exists within the packing. (See Mellor, 1989 for an exposition of this property). The radial distribution function is the simplest measure of crystallinity, and as shown elsewhere in this report, our model sediments exhibit only the short-range order characteristic of dense random packings. Though the grains are randomly arranged, their spatial locations are known. This permits quantifying the mechanical and geometric features that control the phenomena of interest in this project, namely capillarity and solid mechanics.

The packings are **dense**, with porosities 40% or less. In fact for practical purposes the packings are maximally dense, in the sense that no further densification would occur if the algorithms continued to iterate. This is closely analogous to the situation in natural sediments when the grains are coarse enough for mechanical forces (gravity, contact deformation) to be dominant: sand-rich sediments typically have porosities of 35% to 40%. Burial causes sediments to lose porosity by a variety of mechanisms, including grain breakage, pressure solution, and deformation of softer grains. These processes generally have not proceeded appreciably in gas-hydrate bearing formations.

The packings are **load-bearing**, in that application of stress will cause local deformation at grain contacts, per the Hertz-Mindlin theory. Imposing stress will not cause significant re-arrangement of the grains; instead the forces generated by deformation support the imposed load. PFC2D/3D accounts explicitly for the force balance and contact deformation. Its packings are thus in mechanical equilibrium. The cooperative rearrangement packings are not in mechanical equilibrium. Because large forces produce small deformations at contacts between sediment grains, only very small displacements are needed to bring a cooperative rearrangement packing into mechanical equilibrium.

This is why both algorithms yield packings with very similar geometric characteristics. These models can reproduce the macroscopic mechanical behavior of natural sediments, e.g. the axial strain in response to axial stress.

Because of these features, it is well established (Bryant et al., 1993, 1996; Bryant and Raikes, 1995; Bakke and Øren, 1998; Jin et al., 2003; Gladkikh and Bryant, 2005) that dense random packings of spheres capture sufficient geometric features of unconsolidated sands to enable a priori predictions. Macroscopic properties of these sands that depend on grain scale geometry can be predicted without adjustable parameters. Indeed this capability is one of the main motivations for this research project, because it permits a robust assessment of whether a model is capturing the relevant physical phenomena.

Sand-rich sediments

In depositional environments leading to sand-rich sediments, i.e. grains larger than ~50 microns, the sediments commonly exhibit porosities in the range of 30% to 40%, depending on sorting (grain size distribution). Dense random packings of spheres have porosities in the same range. Thus the model sediments are very good facsimiles of coarser grained formations that contain methane hydrates. The delta of the Mackenzie River in Canada is currently the best characterized example of this type of hydrate province. The Mallik well drilled there exhibits porosities averaging 35% in the formations containing hydrates (Guerin and Goldberg, 2002).

Clay-rich sediments

Ocean sediments typically become finer with distance from the shoreline. In many sediments the grain sizes fall into the silt classification (between 2 and 50 microns in diameter) or clays (< 2 microns). In contrast to the silica-rich coarse grains, these fine grains are typically aluminosilicate minerals that have relatively large specific surface area and surface charge density. Because these charged particles are so small, electrostatic forces between particles can be significant. In fact they can contribute to the load-bearing framework. This is in contrast with coarser particles, whose packing is dominated by the stress-strain relationship at particle-particle contacts. As a consequence packings of clay-fraction particles can exhibit larger porosity.

This effect is borne out qualitatively by observations in offshore methane hydrate provinces. For example, a typical shallow Gulf of Mexico sediment is dominated by fine particles of illite less than 10 microns in size, resulting in porosities in the range of 45% to 80% (Francisca et al., 2005.) At Hydrate Ridge, porosities within the hydrate stability zone (HSZ) are typically 50% to 70% (Torres et al., 2004). In a methane-gas filled horizon below the HSZ at Hydrate Ridge, porosities are somewhat smaller, in the range 45% to 55% (Trehu et al, 2004a,b).

Porosities at the low end of these ranges (~45%) can be obtained in "loose" packings of spheres, the load-bearing precursors of "dense" packings which form as the algorithm iterates. But porosities at the high end of the range (>70%) cannot be obtained in load-bearing packings. This does not mean that dense packings cannot be used to model such sediments, however. The sediment porosities reported in the literature are generally

inferred from a determination of the gravimetric water content (Francisca et al., 2005). Because this measurement involves oven drying, it accounts for two types of water: chemically bound water within the clay structure, and water between clay particles. The former occupies microporosity within the solid skeleton formed by the particles. The latter occupies intergranular porosity.

At the capillary pressures attainable in natural systems it is not possible for methane gas to displace water from the microporous void space. Thus only the intergranular porosity is relevant for our application. However, the porosity values inferred from water content lump the microporosity and intergranular porosity together. In clay dominated sediments, the microporosity can be significant fraction of the total porosity. Unfortunately the measurement necessarily destroys the structure of the sediment, so it is difficult to estimate the original intergranular porosity from standard measurements.

How well or how poorly the model sediments created in this Task represent clay-rich sediments thus requires additional empirical information. First, the extent to which electrostatic forces "expand" the framework of clay particles needs to be quantified. We anticipate that the expansion will uniformly increase the intergranular pore throat sizes within the sediment. This correction would be easily accommodated within the process models being developed in other Tasks. Second, the contribution of microporosity to total porosity needs to be measured for typical ocean sediments. Once this is quantified, the influence of other potential factors such as particle shape (platelets rather than spheres) can be properly assessed. In any event, the model sediments will correctly capture the competition between capillarity and grain-grain mechanics, and this competition will govern behavior whatever the details of the pore throat size distribution.

Geometric Properties of the Model Sediments

The PFC2D models are useful for indicating the applicability of the approach for grain-scale mechanics, but they do not represent the pore geometry of 3D sediments. Thus we report the geometric properties only of the cooperative rearrangement packings. Properties of interest include porosity, grain size distribution, radial distribution function and pore throat size distribution. The results of more than 75 runs of our cooperative rearrangement code have been used for this purpose.

The packings each contain 5000 spheres. All are periodic, with a cube as the unit cell. The mean sphere size in each packing is reported in the same units as the unit cube size. Because these units are arbitrary, it is natural to normalize all lengths (in the model sediments by the mean sphere size. The sphere radii in a packing are distributed either normally or log-normally (see Table 1) with different means and standard deviations and consequently different sorting indexes S_o (see Appendix for discussion of S_o). The sorting index is commonly used by sedimentologists and is defined by

$$S_o = \sqrt{\frac{d_{75}}{d_{25}}}$$

where d_{75} is the grain size that is larger than 75% of all grains, and d_{25} is the grain size larger than 25% of all grains. The sorting index is essentially a proxy for the standard deviation of the grain size distribution. The percentage can be calculated on a number fraction basis or on a volume fraction basis. We report both measures. The index can be correlated to the qualitative terminology in customary use as follows:

Extremely well sorted:	$1.0 \leq$ sorting index ≤ 1.1
Very well sorted:	$1.1 \leq$ sorting index ≤ 1.2
Well sorted:	$1.2 \leq$ sorting index ≤ 1.4
Moderately sorted:	$1.4 \leq$ sorting index ≤ 2
Poorly sorted:	$2 <$ sorting index

A summary of the packings is tabulated below. Several realizations were created for each value of sorting index. The shaded rows marked "average" give the average values for the set of realizations immediately above that row. The column labeled "Notes" indicates whether the packing grain size distribution is log normal (LN) or normal (N) and whether the realization exhibits a truncated distribution (Trn) because of the number of spheres used to create the packing.

Table 1. Summary of Properties of Model Sediments							
Grain sizes (arbitrary units)				Porosity (fraction)	Sorting Index		Notes*
Packing No.	Minimum Radius	Maximum radius	Mean radius	Standard deviation		Number fraction basis	Volume or weight fraction basis	
1	0.32	2.58	2.18	0.11	0.37	1.04	1.04	LN
2	1.84	2.64	2.18	0.11	0.36	1.03	1.03	LN
3	1.80	2.60	2.18	0.11	0.37	1.03	1.03	LN

4	0.32	2.59	2.18	0.11	0.35	1.03	1.03	LN
5	1.82	2.52	2.15	0.11	0.41	1.03	1.03	LN
Average	1.22	2.59	2.17	0.11	0.37	1.03	1.03	
6	1.50	3.22	2.17	0.22	0.36	1.07	1.07	LN
7	1.50	3.08	2.16	0.22	0.36	1.07	1.07	LN
8	1.48	2.99	2.17	0.22	0.36	1.07	1.07	LN
9	1.47	3.06	2.16	0.22	0.37	1.07	1.07	LN
Average	1.49	3.09	2.16	0.22	0.36	1.07	1.07	
10	0.96	4.12	2.12	0.42	0.35	1.14	1.14	LN
11	0.93	4.64	2.12	0.43	0.34	1.14	1.14	LN
12	1.07	4.49	2.11	0.42	0.35	1.14	1.14	LN
13	0.99	4.27	2.11	0.43	0.35	1.14	1.14	LN
Average	0.99	4.38	2.11	0.43	0.35	1.14	1.14	
14	4.24E-03	7.05	1.90	0.80	0.32	1.31	1.32	LN
15	3.44E-03	6.44	1.90	0.79	0.35	1.31	1.31	LN
16	3.91E-01	6.38	1.91	0.78	0.33	1.31	1.29	LN
17	7.81E-03	7.01	1.90	0.79	0.32	1.31	1.30	LN
18	1.59E-03	7.62	1.91	0.79	0.32	1.31	1.29	LN
Average	8.17E-02	6.90	1.90	0.79	0.33	1.31	1.30	
19	1.86E-03	11.30	1.31	1.16	0.29	1.72	1.48	LN; Trn
20	2.39E-03	10.16	1.31	1.17	0.25	1.72	1.54	LN; Trn
21	7.85E-03	11.26	1.31	1.15	0.30	1.72	1.53	LN; Trn
22	1.17E-03	11.17	1.30	1.16	0.30	1.69	1.53	LN; Trn
Average	3.32E-03	10.97	1.31	1.16	0.29	1.71	1.52	
23	3.45E-05	11.31	0.69	1.25	0.31	3.11	1.32	LN; Trn
24	1.63E-05	11.19	0.71	1.26	0.30	3.12	1.38	LN; Trn
25	3.80E-05	11.28	0.70	1.25	0.37	3.16	1.30	LN; Trn
26	1.44E-05	12.16	0.72	1.23	0.32	3.07	1.46	LN; Trn
Average	2.58E-05	11.49	0.71	1.25	0.33	3.11	1.37	
27	8.10E-06	18.29	0.30	1.07	0.31	3.63	1.38	LN; Trn
28	2.04E-06	21.32	0.30	1.04	0.29	3.77	1.37	LN; Trn
29	6.94E-06	22.46	0.31	1.04	0.32	3.95	1.41	LN; Trn
Average	5.69E-06	20.69	0.31	1.05	0.31	3.79	1.39	
30	1.24E-03	11.93	1.01	1.20	0.29	2.00	1.50	LN; Trn
31	6.31E-04	11.99	1.04	1.22	0.32	2.00	1.56	LN; Trn
32	5.70E-04	12.34	1.02	1.21	0.30	2.03	1.48	LN; Trn
33	4.21E-05	12.57	1.07	1.22	0.31	1.94	1.51	LN; Trn
34	5.47E-04	11.63	1.03	1.19	0.34	2.01	1.49	LN; Trn
Average	6.06E-04	12.09	1.03	1.21	0.31	2.00	1.51	
35	4.62E-04	9.67	1.63	1.03	0.30	1.51	1.40	LN
36	1.89E-03	9.70	1.61	1.04	0.30	1.50	1.43	LN
37	1.35E-03	9.30	1.59	1.04	0.27	1.49	1.46	LN
38	3.98E-03	9.41	1.60	1.05	0.27	1.51	1.44	LN
Average	1.92E-03	9.52	1.60	1.04	0.29	1.50	1.43	
39	1.97	2.40	2.19	0.07	0.34	1.02	1.02	N

40	1.97	2.41	2.19	0.07	0.35	1.02	1.02	N
41	1.95	2.39	2.17	0.07	0.38	1.02	1.02	N
42	1.97	2.40	2.19	0.07	0.37	1.02	1.02	N
Averages	1.97	2.40	2.18	0.07	0.36	1.02	1.02	
43	1.07	3.20	2.14	0.35	0.36	1.12	1.10	N
44	1.07	3.20	2.14	0.35	0.36	1.12	1.10	N
45	1.07	3.20	2.14	0.36	0.35	1.12	1.11	N
46	1.07	3.20	2.14	0.35	0.37	1.12	1.11	N
Averages	1.07	3.20	2.14	0.35	0.36	1.12	1.10	
47	5.64E-05	4.01	2.01	0.68	0.34	1.27	1.17	N
48	4.20E-05	4.01	2.01	0.66	0.33	1.25	1.17	N
49	3.59E-05	4.03	2.01	0.67	0.34	1.25	1.18	N
50	3.22E-05	4.04	2.02	0.66	0.33	1.25	1.17	N
Averages	4.16E-05	4.02	2.01	0.67	0.34	1.26	1.17	
51	1.27E-03	4.59	1.85	0.90	0.32	1.42	1.21	N
52	1.10E-03	4.51	1.85	0.91	0.34	1.42	1.21	N
53	5.94E-04	4.44	1.86	0.89	0.35	1.40	1.21	N
54	2.94E-03	4.59	1.86	0.90	0.32	1.42	1.20	N
Averages	1.48E-03	4.53	1.86	0.90	0.33	1.42	1.21	
55	6.34E-04	5.00	1.73	1.04	0.32	1.60	1.23	N
56	3.30E-04	5.06	1.71	1.05	0.31	1.64	1.22	N
57	1.56E-03	5.07	1.71	1.05	0.35	1.62	1.22	N
58	8.76E-04	5.08	1.71	1.05	0.34	1.65	1.23	N
59	1.09E-03	5.01	1.70	1.05	0.33	1.63	1.22	N
Averages	8.98E-04	5.04	1.71	1.05	0.33	1.63	1.22	
60	3.81E-03	4.56	1.84	0.91	0.32	1.43	1.21	N
61	4.85E-03	4.82	1.77	1.00	0.31	1.53	1.22	N
62	4.93E-03	4.85	1.76	1.00	0.35	1.53	1.23	N
63	4.47E-04	4.81	1.76	1.00	0.33	1.53	1.22	N
64	2.51E-03	4.82	1.77	0.99	0.33	1.51	1.22	N
65	4.94E-03	4.88	1.76	1.00	0.34	1.54	1.23	N
Averages	3.58E-03	4.79	1.78	0.98	0.33	1.51	1.22	
66	3.31E-03	5.36	1.60	1.15	0.33	1.89	1.24	N
67	1.88E-04	5.38	1.61	1.14	0.32	1.85	1.24	N
68	2.30E-03	5.44	1.60	1.15	0.33	1.94	1.23	N
69	2.37E-03	5.43	1.60	1.14	0.33	1.91	1.24	N
70	2.43E-04	5.32	1.59	1.14	0.33	1.90	1.25	N
Averages	1.68E-03	5.39	1.60	1.14	0.33	1.90	1.24	
71	2.88E-04	5.46	1.54	1.19	0.33	2.12	1.23	N
72	2.93E-03	5.47	1.53	1.20	0.33	2.20	1.23	N
73	2.86E-04	5.49	1.52	1.20	0.32	2.27	1.24	N
74	2.52E-03	5.64	1.53	1.20	0.33	2.18	1.24	N
75	8.97E-04	5.65	1.53	1.19	0.33	2.13	1.26	N
76	7.35E-04	5.52	1.53	1.20	0.32	2.23	1.24	N
Averages	1.28E-03	5.54	1.53	1.20	0.32	2.19	1.24	

[*]LN = log normal distribution of sphere sizes. N = normal distribution of sphere sizes. Trn indicates that the actual distribution of sphere sizes in the packing was truncated.

Effect of sorting on packing porosity

The experiments of Beard and Weyl (1973) show that porosity decreases as sorting index increases. Our packings show the same trend as the data for $S_o < 2$. As discussed below, our packings do not have enough spheres to reproduce the statistics of sediments with S_o

> 1.5, so the deviations at large sorting are expected. The absolute values of porosity are about 5 percentage points smaller than the sand pack data. This is consistent with the fact that our packings are maximally dense and do not account for the effects of angular grains, which hinder settling into dense packings.

Table 2. Measurements of wet-packed sand porosity for different grain size distributions (Beard and Weyl, 1973).	
Sorting Index	Porosity
1.05	0.42375
1.15	0.40788
1.3	0.39013
1.7	0.33963
2.35	0.30725
4.2	0.27275
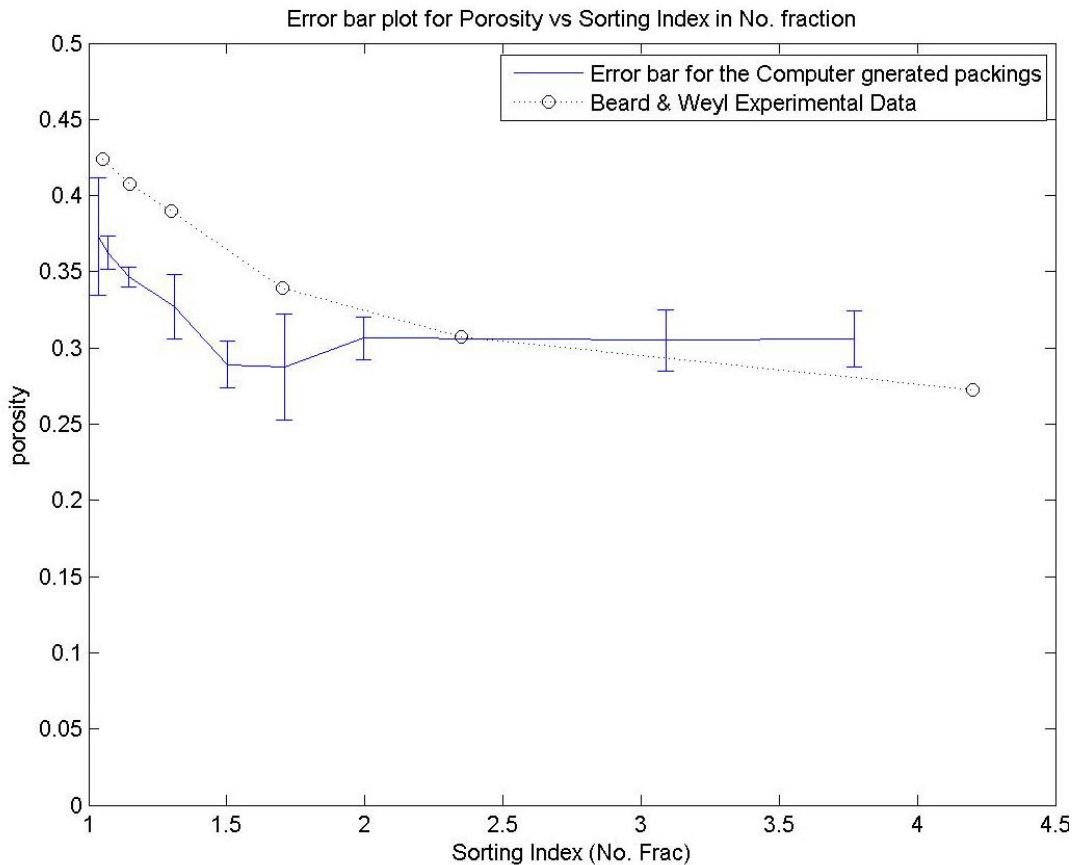
Figure 21. Model sediments with log normal grain size distributions show similar trend in porosity vs. sorting to the measurements of Beard and Weyl (1973) for $S_o < 2$. The sorting index is computed using number fraction of spheres.
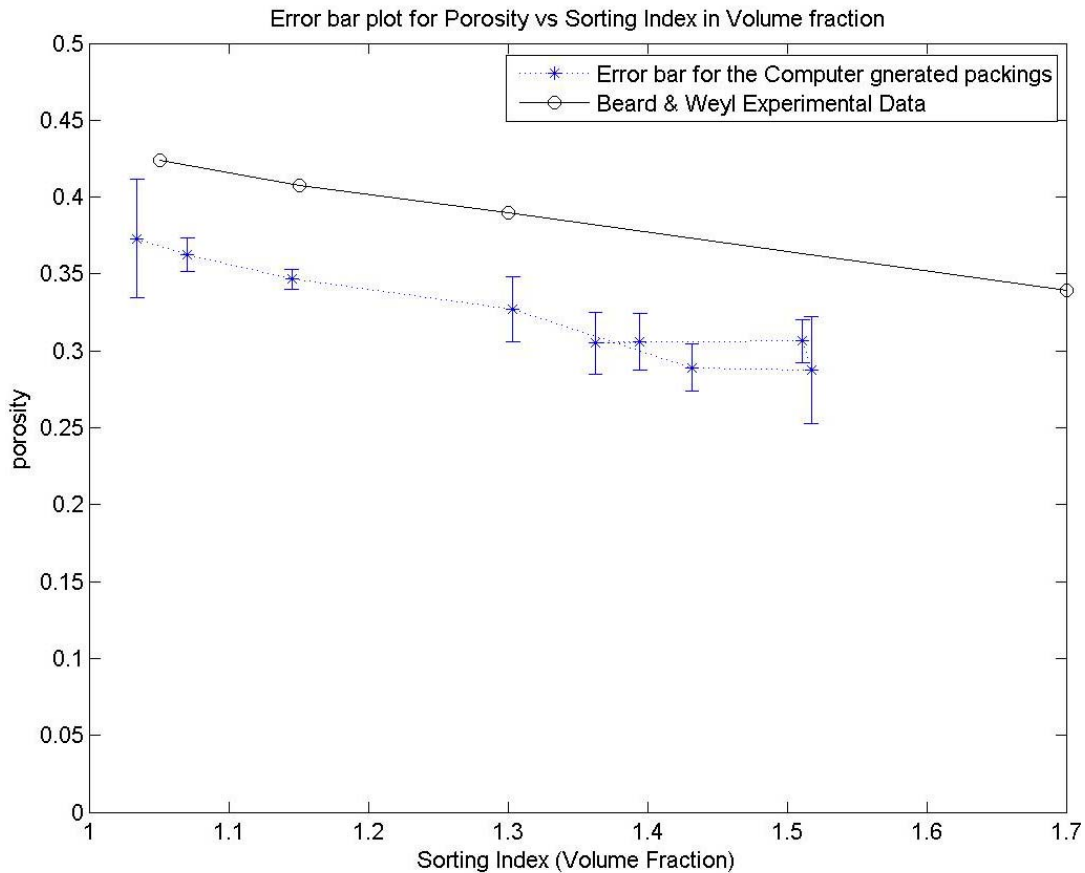
Figure 22. When the sorting index is computed using volume fraction of spheres, the model sediments of Fig. 21 again show a trend in porosity vs. sorting similar to the measurements of Beard and Weyl (1973) for $S_o < 1.5$.

Limitation on range of sorting in the packings

All cooperative rearrangement packings were constructed with 5000 spheres. This number has been found adequate for capturing the essential geometric features in well sorted packings (Thane, 2006). For packings with log normal size distributions of sphere sizes, the ratio of diameters of large and small spheres grows rapidly as standard deviation of the distribution increases. It is thus important to check the grain size distribution of actual packing against the prescribed distribution.

The following plots show how the weight percent distribution of sphere sizes in packings produced by cooperative rearrangement changes as we increase the sorting index. Also we have included the CDF achieved using the weight percent to compare with CDFs based on number fraction and volume fraction. For sorting index greater than 1.5, the number of grains in the packing is too small to reproduce the statistics of the prescribed log normal distribution. In particular, not enough large spheres occur in the packing, and the grain size distribution in the packing is truncated above. We include data on the packings having S_o larger than 1.5 for reference, but only the packings with S_o less than or equal to 1.5 can be regarded as good model sediments.

27

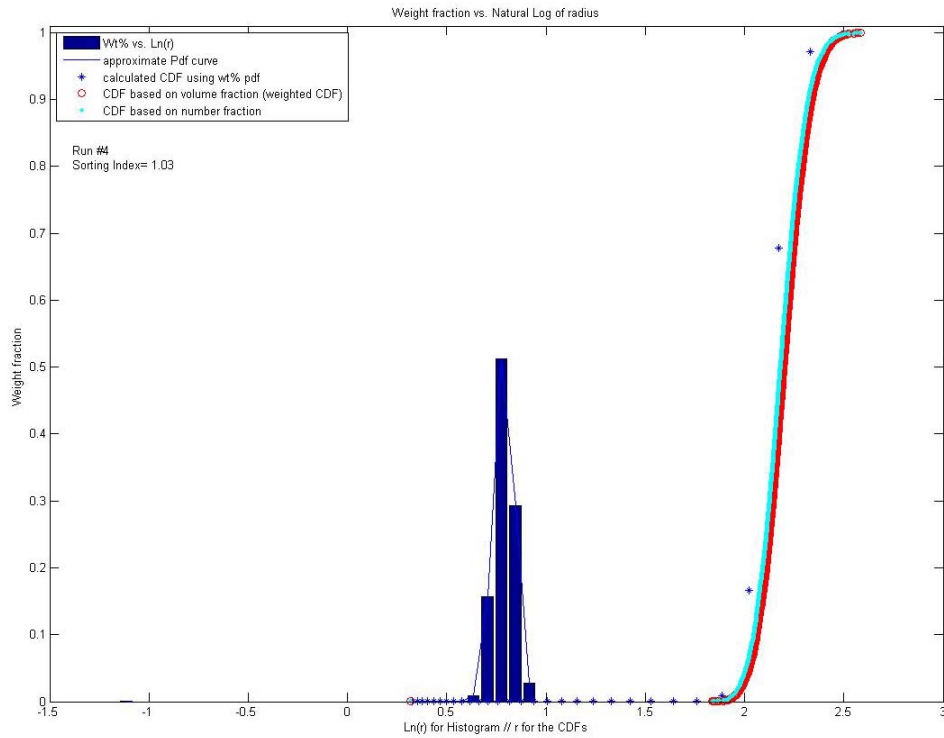Images of subvolumes of several representative packings can be found in the Appendix.

Figure 23. Weight fraction vs. Natural Log of radius (Sorting index = 1.03)
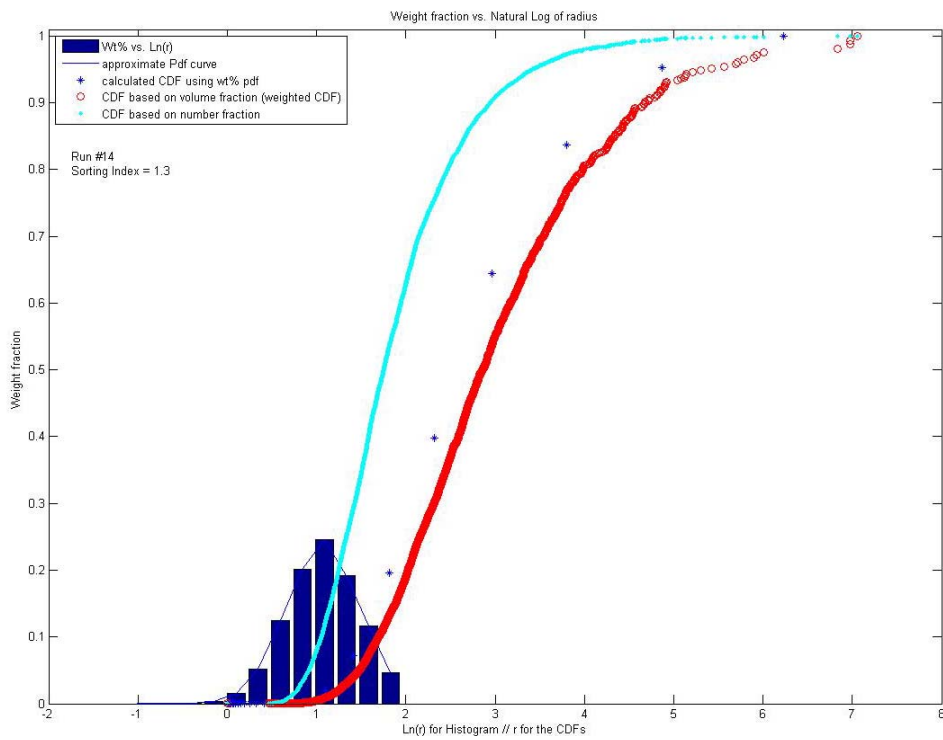

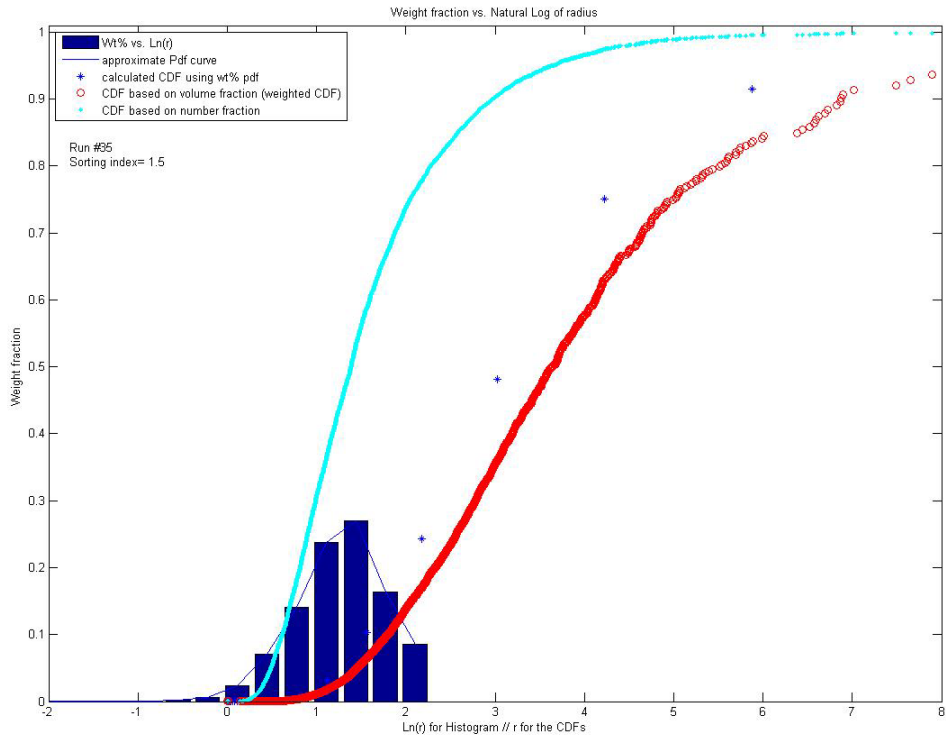**Figure 24. Weight fraction vs. Natural Log of radius (Sorting index = 1.3)**

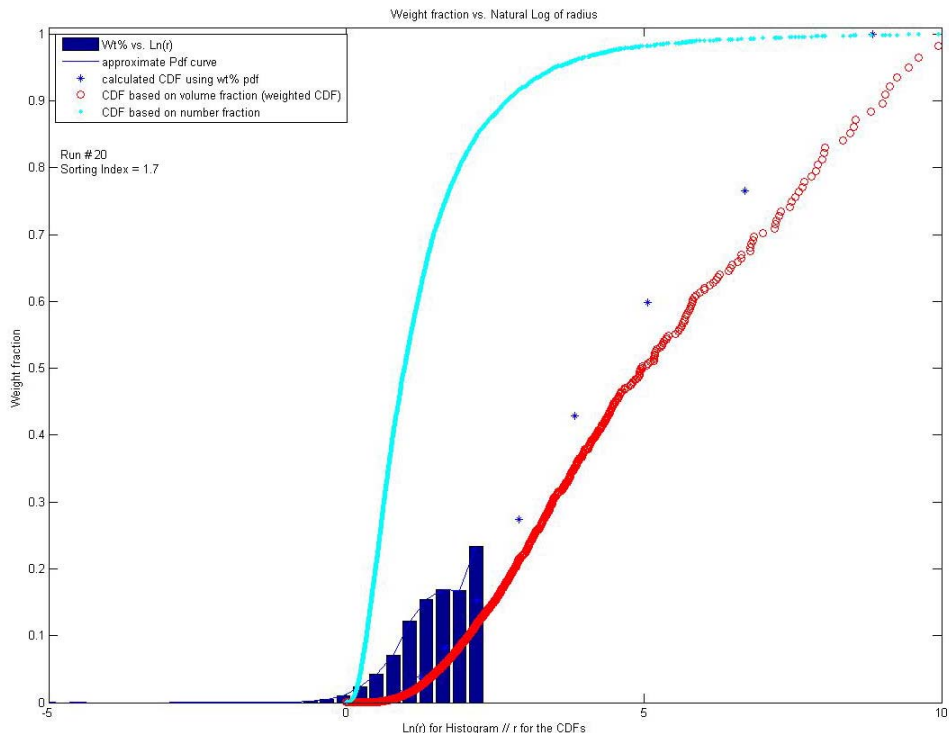**Figure 25. Weight fraction vs. Natural Log of radius (Sorting index = 1.5)**

Figure 26. Weight fraction vs. Natural Log of radius (Sorting index = 1.7)
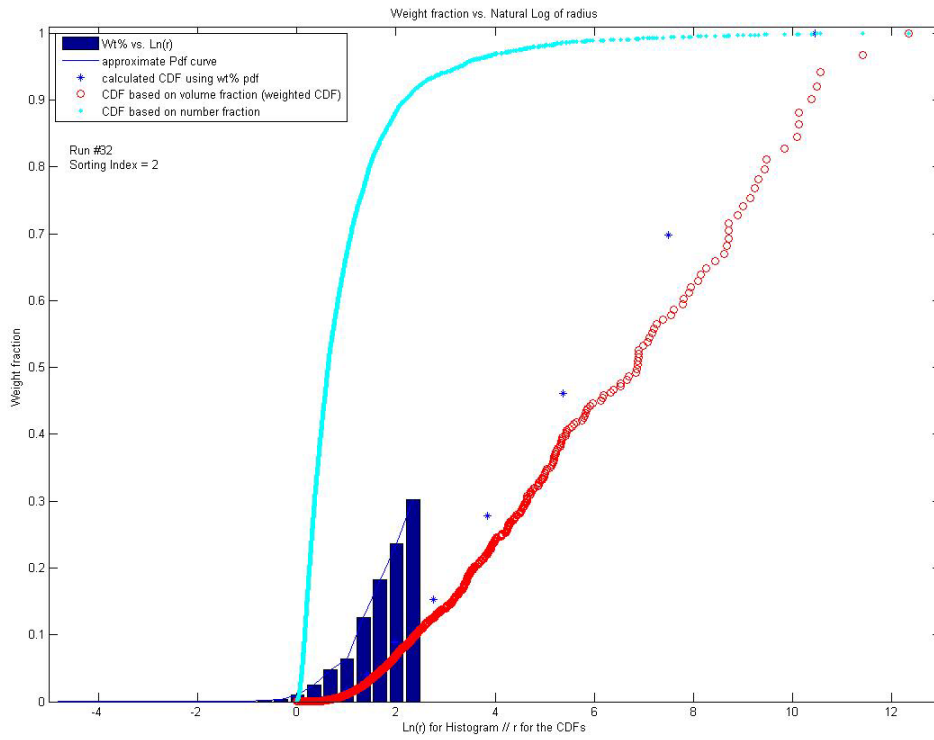
Figure 27. Weight fraction vs. Natural Log of radius (Sorting index = 2)
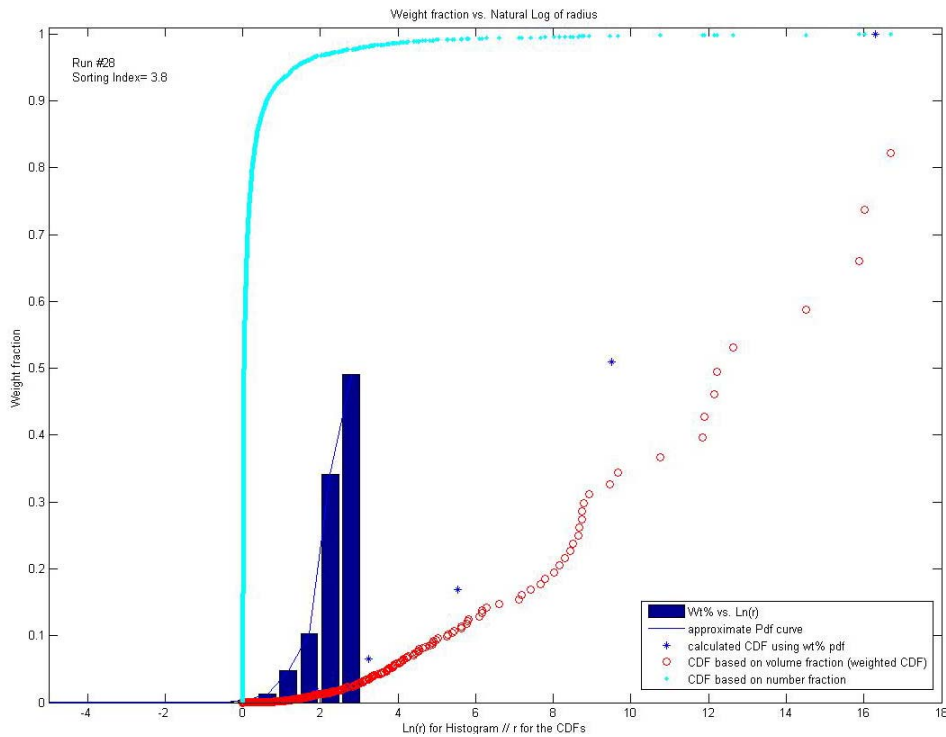

Figure 28. Weight fraction vs. Natural Log of radius (Sorting index = 3.8)

30

Radial Distribution Function

The radial distribution function (RDF) is convenient measure of structure in a packing. The function measures the probability of finding another sphere at a prescribed distance from an arbitrary test sphere. Peaks in the function correspond to common arrangements of spheres, while valleys indicate relatively rare arrangements. At sufficiently large distances within a random packing, the function approaches the average number density of spheres in the packing. The distance at which the peaks and valleys die out thus corresponds to a correlation length. RDFs for the model sediments corresponding to Figs. 23-25 above are shown below, along with the corresponding grain size distribution. The complete set of RDFs is available in the Appendix.
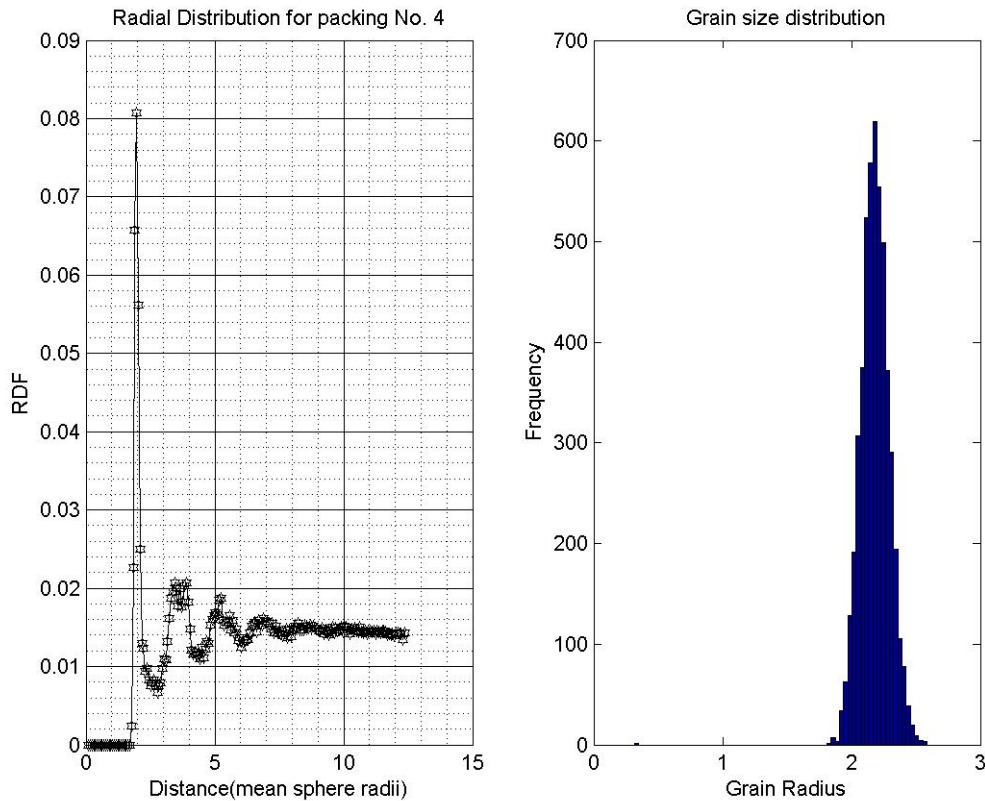

Figure 29. (left) Radial distribution function (RDF) for extremely well sorted model sediment, packing No. 4. The peak at distance = 2 corresponds to spheres in point contact. Structure indicated by peaks and valleys in the RDF decays within about 7 sphere radii. The peaks correspond to common configurations such as three spheres in mutual contact. (right) Grain size distribution for the same packing.
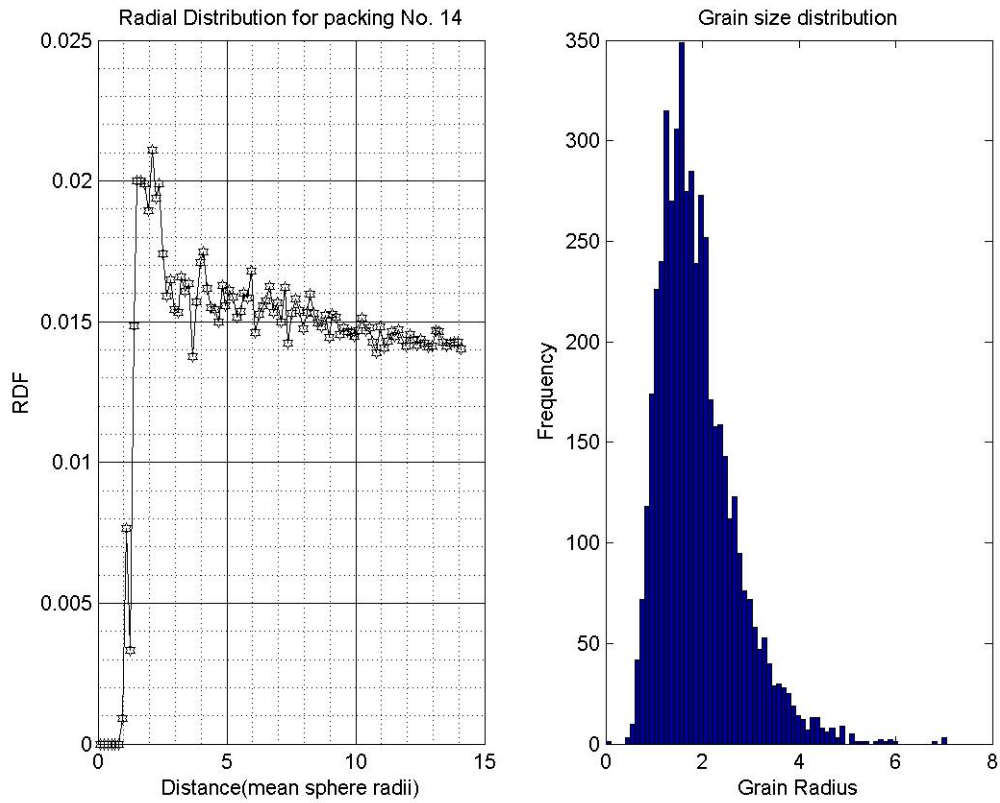
31

Figure 30. (left) Radial distribution function (RDF) for well sorted model sediment, packing No. 14. The peak at distance = 2 corresponds to spheres in point contact. There is much less short-range structure compared to the extremely well sorted packing of Fig. 29. (right) Grain size distribution for the same packing.
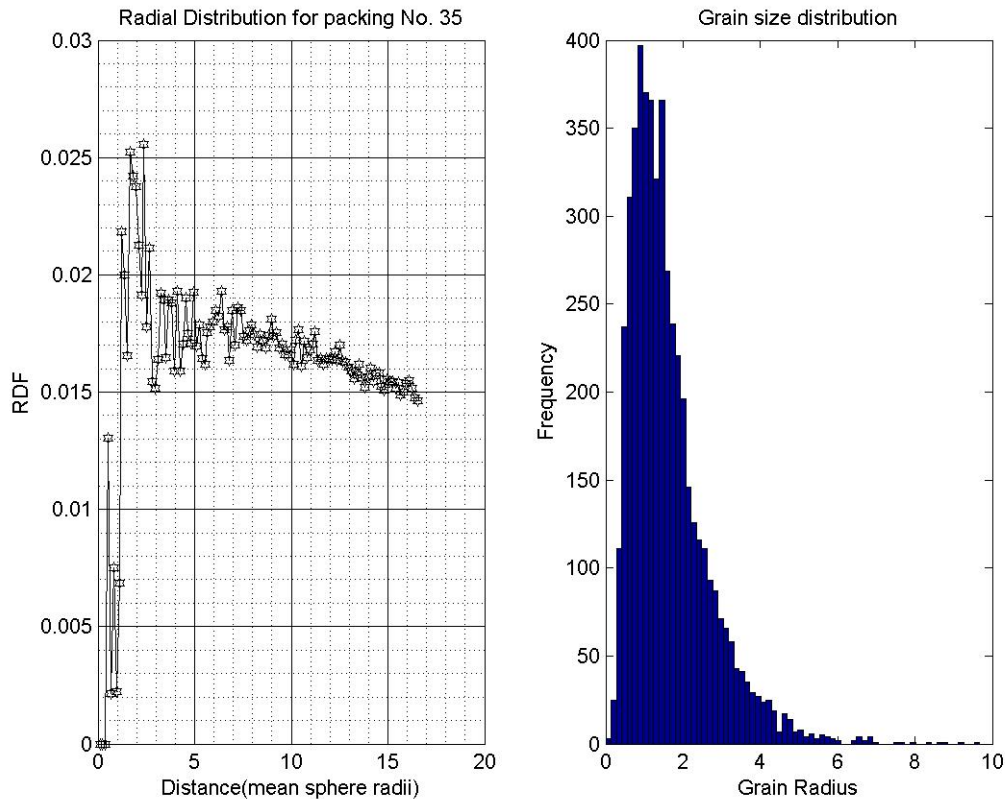
Figure 31. (left) Radial distribution function (RDF) for moderately sorted model sediment, packing No. 35. Compared to better sorted packings, even the peak at distance = 2 is less distinct. The RDF decays to the average packing density of 0.015 with few discernible peaks or valleys, indicating an essentially random structure. (right) Grain size distribution for the same packing.

Pore Space Network Properties of the Model Sediments

Pore Throat Size Distribution

A convenient method for identifying pores in a packing of spheres is the Delaunay tessellation of the sphere centers. The dual of the Voronoi tessellation, the Delaunay tessellation groups together sets of nearest neighbor spheres. Each set contains four spheres. The operational definition of "nearest neighbors" is based on the circumsphere defined by the centers of the four neighbors. If this circumsphere does not contain the center of any other sphere in the packing in its interior, then the neighbors are indeed nearest neighbors.

The centers of a set of nearest neighbors defines a tetrahedron. The void area in the faces of this tetrahedron is locally the narrowest constriction in pore space. It thus controls access to the interior of the tetrahedron and corresponds to a pore throat. As the distribution of grain sizes becomes broader, the geometry of the hydraulically relevant pore throat may be determined by the arrangement of additional sphere(s) in the vicinity

of those defined by the Delaunay tessellation. For the purposes of comparing features of different packings, however, the sizes of throats in the Delaunay tetrahedral is sufficient.

The figures below show the distributions of throat sizes for the packings corresponding to Figs. 23-25. Each distribution is accompanied by the grain size distribution for the packing so that the effect of sorting on the throat sizes can be more easily assessed. The complete set of distributions is given in the Appendix.
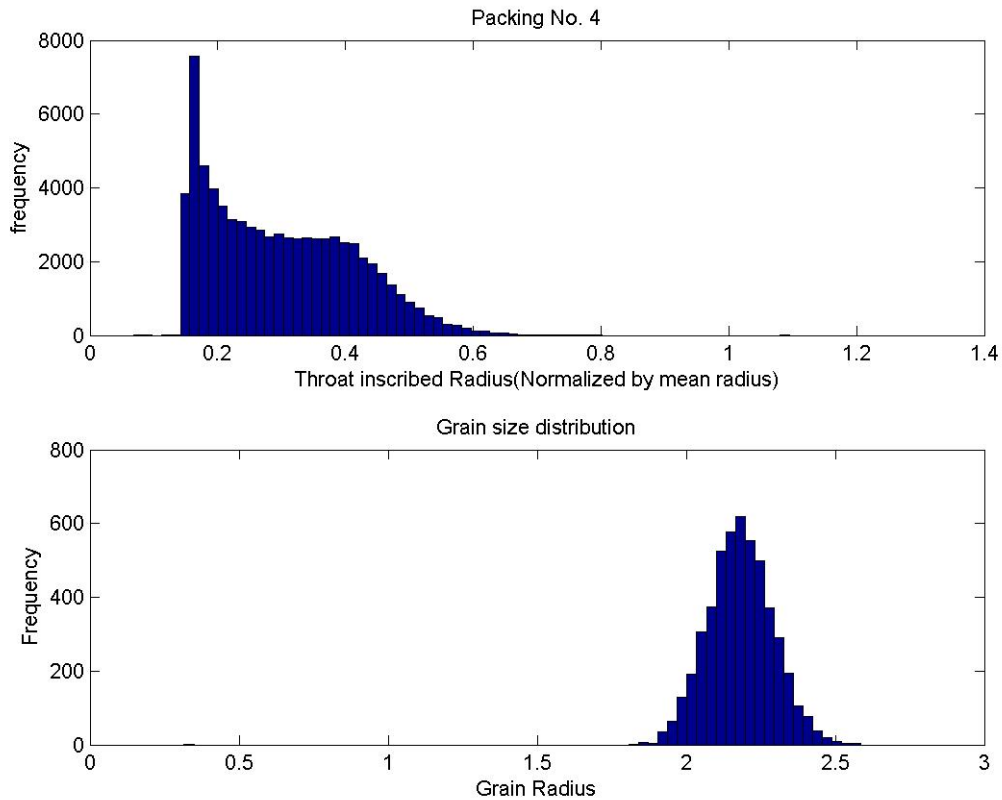

Figure 32. (top) Pore throat size distribution for extremely well sorted model sediment, packing No. 4. The peak at *r* = 0.15 corresponds to the throat between three spheres in point contact. (bottom) Grain size distribution for the same packing.
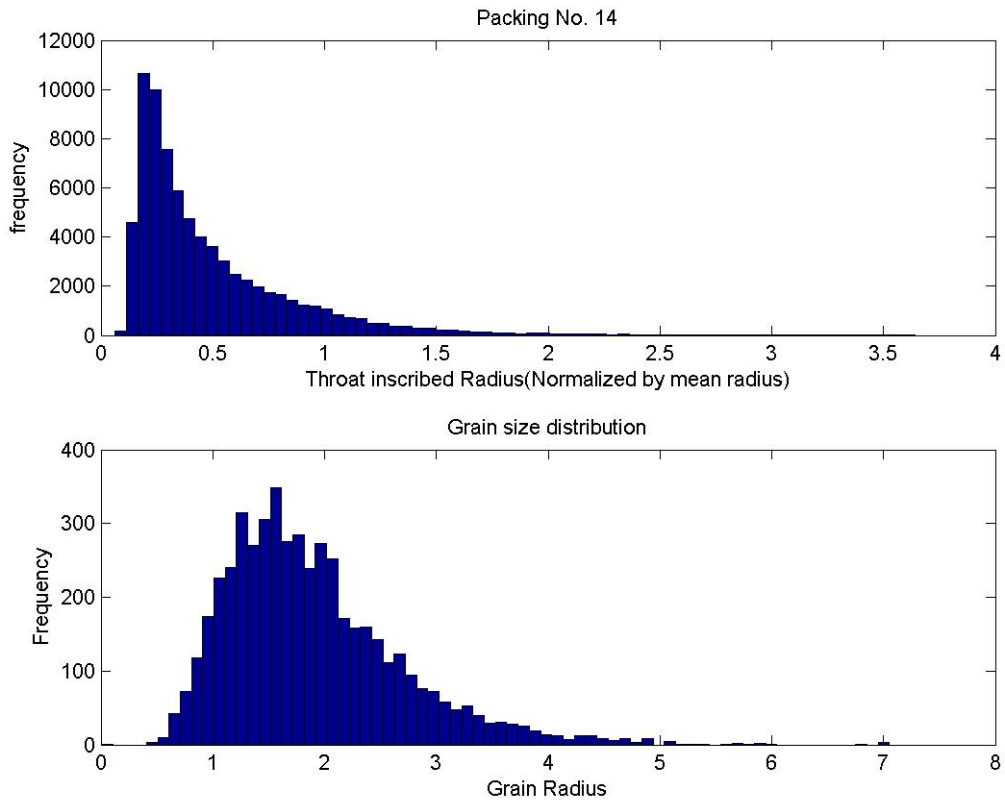
Figure 33. (top) Pore throat size distribution for well sorted model sediment, packing No. 14. The peak at *r* = 0.15 is broader than in the extremely well sorted packing, and the entire distribution is broader as well. (bottom) Grain size distribution for the same packing.
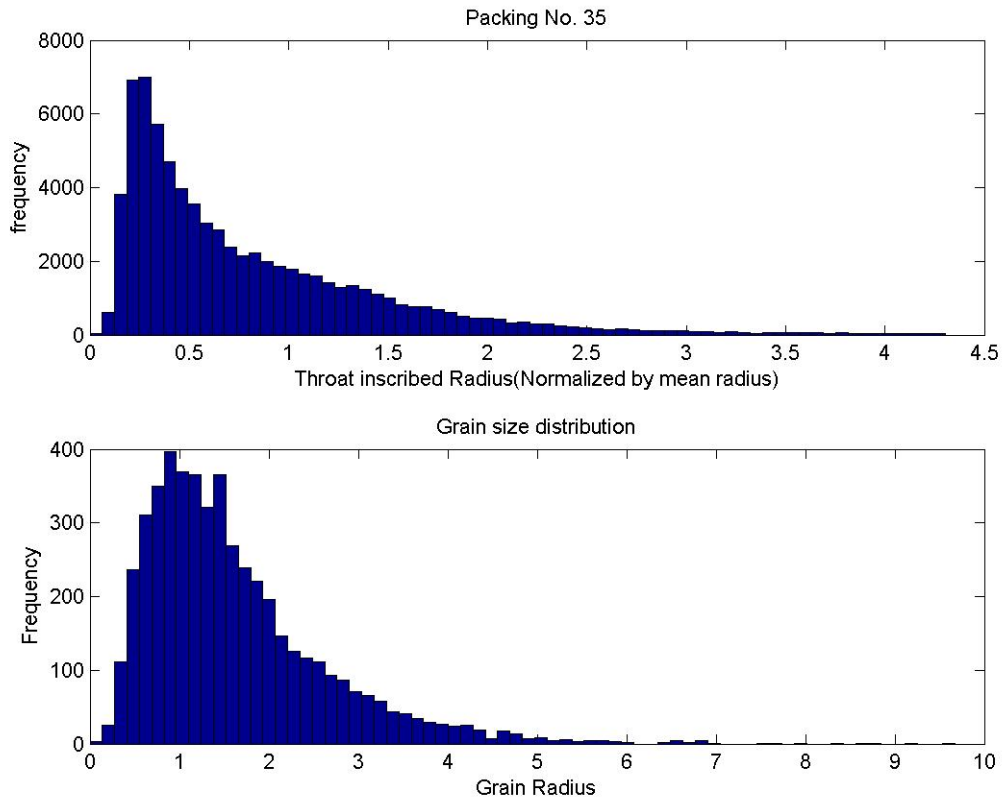
Figure 34. (top) Pore throat size distribution for moderately sorted model sediment, packing No. 35. (bottom) Grain size distribution for the same packing.

Network Topology from Delaunay Tessellation of Sphere Centers

The topology of pore space within the model sediments is readily extracted from the same Delaunay tessellation that identifies pore throats. The process is illustrated schematically below. We will carry out mechanistic simulations of drainage (methane gas displacing brine) and imbibition (brine displacing methane gas) in the networks resulting from tessellation. Because the networks are constructed directly from the geometry of the sphere packing, the displacement events can be mapped directly into pore space. This will enable us to compute quantities such as interfacial area between gas and water phases, where hydrate formation is presumed to start. We will also be able to determine the extent to which gas phase enters or withdraws from the model sediment as a function of capillary pressure. This in turn will be compared to the pore pressure required to alter the structure of the packing. In this way the competition between capillarity and solid mechanics can be quantified.
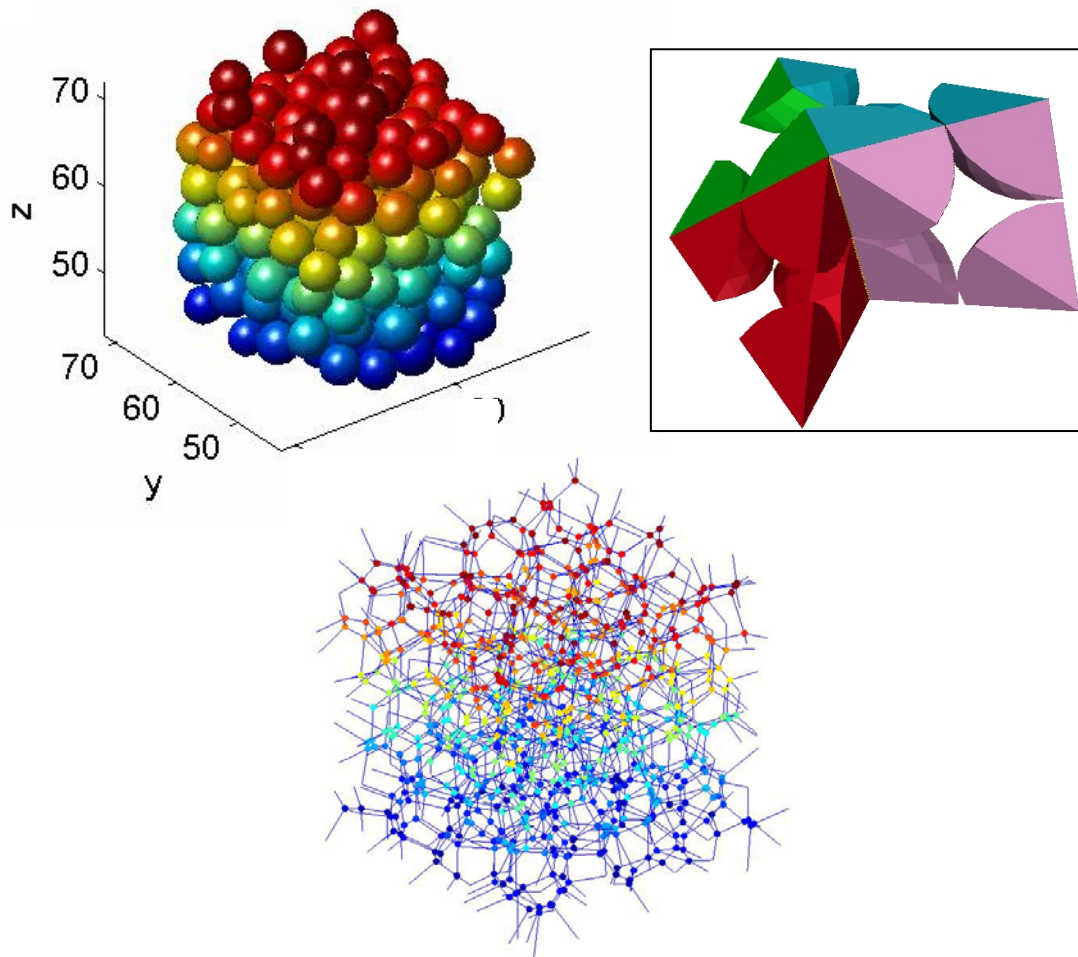
Figure 35. (top left) Dense random packing of extremely well sorted spheres (packing No. 4) generated by cooperative rearrangement algorithm. (top right) Four Delaunay cells from within the packing. Only the segments of spheres within each cell are shown. The interior of each cell corresponds to a pore body. The void space in each triangular face of a cell corresponds to a pore throat. (bottom) The topology of pores within the packing. The colored dots are the locations of centers of pores identified by tessellating the sphere centers. The line segments join neighboring pores. The absence of any regular structure is apparent, though all pores have four throats (because each Delaunay cell is a tetrahedron.) The radius of the throat corresponding to each line segment is known. The capillarity-controlled displacement of brine by methane gas (drainage), or of methane gas by brine (imbibition), can be simulated directly within this network.

Guide to Model Sediment Data Files

There are four sets of text files available for the 76 packings produced by the cooperative rearrangement algorithm and summarized in Table 1.

- **Listing of sphere centers and radii for each packing**
  The file name for this category is "Coordinates_PackingNN.txt" where NN indicates the number of the packing in Table 1. For example the file named

"`Coordinates_Packing12.txt`" includes the X, Y and Z coordinates of the centers of the spheres making up the packing and also the radius of the spheres for the 12th packing. The coordinates are in the same arbitrary but self-consistent units used to report grain sizes. There are 4 columns in each of these text files. The first 3 columns are XYZ coordinates of the sphere centers respectively and the fourth column contains the radius of the corresponding spheres. The ID number for each sphere is the number of the row the data of that specific sphere is mentioned. This ID number is used to refer to the spheres in the Delaunay tessellation (see next file type).

Example: the first ten lines of `Coordinates_Packing1.txt` are shown below

```
2.9510300e+001   2.1302500e+001   4.0295900e+001   2.2783500e+000
5.3711700e+001   1.2861000e+001   4.3209600e+001   2.2168100e+000
6.6300900e+001   6.5553900e+001   1.8227200e+001   2.1118800e+000
9.6867900e+000   6.1662900e+000   2.9074100e+001   2.2594700e+000
2.4610100e+001   2.4928900e+001   1.6943900e+001   2.1263300e+000
1.3072500e+001   2.2058300e+001   1.2149000e+001   2.1046600e+000
5.0956900e+001   3.7340800e+001   2.4290000e+000   2.3653800e+000
7.0123200e+000   4.4366600e+001   2.6550400e+001   2.1209200e+000
2.5703100e+001   1.4560700e+001   6.3361000e+001   2.1258700e+000
6.6219300e+001   3.4782600e+001   5.1609200e+001   2.1561500e+000
```

Thus sphere 1 in this packing has radius 2.27835 and its center is located at (29.5103, 21.3025,40.2959).

- **Listing of sphere IDs corresponding to Delaunay tessellation for each packing**

The file name is "`Tes_Matrix_PackNN.txt`" where `NN` indicates the packing number in Table 1. It includes four columns. Each row in this text file represents a Delaunay cell. The four numbers mentioned in each row indicate the IDs of the spheres that make up a Delaunay cell. The number of each row is the ID number for the corresponding Delaunay cell. This ID number is used in the topology file (see next file type).

Example: the first ten lines of `Tes_Matrix_Pack1.txt` are shown below.

```
2.8910000e+003   3.2660000e+003   2.5230000e+003   4.8480000e+003
2.4040000e+003   4.3260000e+003   1.2230000e+003   2.5280000e+003
3.3540000e+003   1.2910000e+003   3.9550000e+003   4.9920000e+003
1.7380000e+003   4.8110000e+003   7.0900000e+002   4.4200000e+002
6.6900000e+002   1.3730000e+003   3.8360000e+003   4.5170000e+003
6.3000000e+001   3.4640000e+003   4.6450000e+003   1.7090000e+003
1.2460000e+003   3.4640000e+003   4.6450000e+003   1.7090000e+003
1.2460000e+003   2.1210000e+003   3.4640000e+003   1.7090000e+003
2.8360000e+003   2.8910000e+003   3.2660000e+003   2.5230000e+003
4.3630000e+003   3.5390000e+003   4.5110000e+003   2.5380000e+003
```

Thus the first Delaunay cell corresponds to spheres 2891, 3266, 2523 and 4848. By inspecting the corresponding lines of file `Coordinates_Packing1.txt`, we could determine the spatial location of each corner of this tetrahedron, and thus the radii of each pore throat in this cell. Note that cells 6 and 7 both contain spheres 3464, 4645 and 1709. This means that cells 6 and 7 will be neighbors (see topology file next). Similarly, cell 1 and cell 9 have three spheres in common, namely 2891, 3266 and 2523.

- **Listing of network topology (which cells in the above file are the neighbors of each cell)**

The file name is "`Neighbors_Matrix_PackNN.txt`" where `NN` indicates the packing number in Table 1. This file contains four columns. Each row corresponds to one cell in the tessellation. Each column contains the ID number of a cell that neighbors the given cell. There are four columns, because all cells are tetrahedral and therefore have four neighbors. Though the packings are periodic, this listing treats the packing as though it were finite and limited to the cubic domain used by the cooperative rearrangement algorithm. Thus cells on the outer face of the packing will have less than four neighbors *within* the packing. The exterior face(s) of these cells are assigned a neighbor index of zero (0).

Example: the first ten lines of `Neighbors_Matrix_Pack1.txt` are shown below.

```
9.0000000e+000   1.5300000e+002   0.0000000e+000   0.0000000e+000
1.2000000e+003   3.8980000e+003   3.9410000e+003   3.8130000e+003
1.9750000e+003   8.8300000e+002   0.0000000e+000   0.0000000e+000
2.9000000e+002   1.3110000e+003   4.0350000e+003   8.7830000e+003
1.2400000e+002   1.2200000e+002   5.8490000e+003   0.0000000e+000
7.4500000e+002   7.4800000e+002   3.0400000e+002   7.0000000e+000
2.7220000e+003   1.4300000e+002   8.0000000e+000   6.0000000e+000
6.9680000e+003   7.0000000e+000   2.8850000e+003   3.0300000e+002
1.5400000e+002   2.9100000e+003   2.5000000e+001   1.0000000e+000
1.6000000e+002   7.3600000e+002   4.5000000e+001   2.1762000e+004
```

Thus the first Delaunay cell has as neighbors cells 9, 153, 0 and 0. The latter two mean that the first cell has two faces on the exterior of the packing. The ninth line indicates that cell 9 has neighbors 154, 2910, 25 and 1. The presence of cell 1 in this list serves as a consistency check; we have carried out this check on the topology file for every packing. Similarly, cell 7 is the fourth neighbor of cell 6, and cell 6 is the fourth neighbor of cell 7. To determine the size of the pore throat connecting cells 6 and 7, one would identify the sphere IDs that are common to the Delaunay cell definitions for cells 6 and 7 (see previous section.) The spatial locations and radii of these spheres can be extracted from the file of coordinates. This information is sufficient to determine the radius of the inscribed circle (and any other geometric information desired), which we use as a measure of the pore throat size (see next file type).

- **Listing of pore throat radii associated with each throat connecting neighboring cells**

The file name is "`Normalized_Pore_Throat_Size_Matrix_PackNN.txt`" where `NN` indicates the packing number in Table 1. It includes the normalized pore throat radii associated with each throat connecting neighboring cells throughout the packing. The throat radii in each packing are normalized by the mean sphere radius (see Table 1). Thus the normalization factor differs from packing to packing, but after normalization all quantities involving length are comparable between packings. A radius of −1 indicates a throat that is connected to the exterior of the packing. The treatment of such throats depends on the algorithm to be used for drainage and imbibition. If the actual geometric value is needed, it can be readily extracted from the other three data files as discussed above.

The throat radii file is constructed in exactly the same order as the topology file above. The line number of each row corresponds to the Delaunay cell number. For a given row, the first column contains the radius of the throat connecting the given cell to its first neighbor. (The first neighbor is identified in the corresponding line of the topology file). The second column contains the radius of the throat connected the given cell to the second neighbor, and so on.

Example: the first ten lines of `Normalized_Pore_Throat_Size_Matrix_Pack1.txt` are shown below.

```
1.7554545e-001   1.6062099e-001  -1.0000000e+000  -1.0000000e+000
4.2141740e-001   2.5307557e-001   3.0896714e-001   2.4233366e-001
3.7456316e-001   3.7354064e-001  -1.0000000e+000  -1.0000000e+000
3.1531876e-001   2.2893521e-001   3.1233790e-001   3.7145802e-001
1.4884367e-001   1.5176807e-001   4.1038120e-001  -1.0000000e+000
2.6542254e-001   1.6435000e-001   3.7279741e-001   4.1491201e-001
2.7451845e-001   2.0055349e-001   3.8093278e-001   4.1491201e-001
5.3127678e-001   3.8093278e-001   4.2109478e-001   5.0433782e-001
2.2256290e-001   2.2367991e-001   1.7227901e-001   1.7554545e-001
3.6117889e-001   2.8125971e-001   1.7008389e-001   2.9634619e-001
```

Thus the first Delaunay cell has throats of radius $0.175545R$, $0.160621R$ and two throats connected to the exterior of the packing. Here R is the mean radius of spheres in packing No. 1, which is 2.18 (cf. Table 1). Cell 10 is connected to its neighbors through throats of radius $0.361179R$, $0.28126R$, $0.170084R$ and $0.296346R$. Cell 6 is connected cell 7 through a throat of radius $0.414912R$, i.e. through the fourth throat of cell 6.

REFERENCES

Bakke, S. and P. Øren: "Extending predictive capabilities to network models," *Soc. Pet. Eng. J.* **3**:324-336, 1998.

Beard, D. C., and P. K. Weyl, 1973, Influence of texture on porosity and permeability of unconsolidated sand. American Association of Petroleum Geologists Bulletin, v. 57, p. 349-369.

M. S. Bruno and R. B. Nelson. Microstructural analysis of the inelastic behavior of sedimentary rock. *Mech. Mater.*, 12(2):95–118, 1991.

M. S. Bruno. Micromechanics of stress-induced permeability anisotropy and damage in sedimentary rocks. *Mech. Mater.*, 18:31–48, 1994.

S. Bryant, C. Cade, and D. Mellor. Physically representative network models of transport in porous media. *AIChE J.*, 39:387–396, 1993.

S. Bryant, G. Mason, and D. Mellor. Quantification of spatial correlation in porous media and its effect on mercury porosimetry. *J. Colloid Interface Sci.*, 177:88–100, 1996.

S. Bryant and S. Raikes: "Prediction of elastic wave velocities in sandstones using structural models," *Geophysics* **60**:437-446, 1995.

P. A. Cundall and O. D. L. Strack. Discrete numerical model for granular assemblies. *Geotechnique*, 29:47–65, 1979.

P. B. Flemings, X. Liu, and W. J. Winters. Critical pressure and multiphase flow in Blake Ridge gas hydrates. *Geology*, 31(12):1057–1060, 2003.

Francisca et al, 2005. "Geophysical and geotechnical properties of near-seafloor sediments in the northern Gulf of Mexico gas hydrate province". Earth and Planetary Science Letters, Volume 237 924–939.

Ginsburg et al, 2000. "Sediment Grain-Size Control On Gas Hydrate Presence, Sites 994, 995, And 997". Proceedings of the Ocean Drilling Program, Scientific Results, Volume 164.

M. Gladkikh and S. Bryant. Prediction of imbibition in unconsolidated granular materials. *J. Colloid Interface Sci.*, 288:526–539, 2005.

Gracia et al, 2006. "Data Report: Sediment Grain-Size and Mineralogy". Proceedings of the Ocean Drilling Program, Scientific Results, Volume 204.

G. Guerin and D. Goldberg, "Sonic waveform attenuation in gas hydrate-bearing sediments from the Mallik 2L-38 research well, Mackenzie Delta, Canada," *J. Geophys. Res.* **107**(B5), 10.1029/2001JB000556, 2002.

ITASCA. *PFC3D, v3.1 – Theory and Background*. Itasca Consulting Group, Inc., Minneapolis, MN, 2005.

G. Jin. *Physics-Based Modeling of Sedimentary Rock Formation and Prediction of Transport Properties*. PhD Dissertation, University of California at Berkeley, Spring 2006.

G. Jin, T. W. Patzek, and D. B. Silin. Physics based reconstruction of sedimentary rocks. In *SPE Western Regional/AAPG Pacific Section Joint Meeting*, Long Beach, CA, May 19–24 2003. (SPE 83587).

Mellor, D. *Random close packing of equal spheres: structure and implications for use as a model porous medium*, Ph.D dissertation, Open University, 1989.

Paull, C.K, R. Matsumoto, P.J. Wallace et al. Proceedings of the Ocean Drilling Program, Initial Reports, vol. 164, Ocean Drilling Program, College Station, TX, 1996.

M. Riedel, P. Long, C.S. Liu, P. Schultheiss, T. Collett, and ODP Leg 204 Shipboard, 2006. "Physical Properties of Near-Surface Sediments at Southern Hydrate Ridge: Results from ODP Leg 204". Proceedings of the Ocean Drilling Program, Scientific Results, Volume 204.

Tan et al, 2006. "Data Report: Consolidation and Strength Characteristics of Sediments from ODP Site 1244, Hydrate Ridge, Cascadia Continental Margin". Proceedings of the Ocean Drilling Program, Scientific Results, Volume 204.

Thane, C. "Geometry and Topology of Model Sediments and Their Influence on Sediment Properties," M.S. Thesis, The University of Texas at Austin, 2006.

M. E. Torres, K. Wallman, A. M. Trehu, G. Bohrmann, W. S. Borowski, and H. Tomaru. Gas hydrate growth, methane transport, and chloride enrichment at the southern summit of Hydrate Ridge, Cascadia margin off Oregon. *Earth Planet. Sci. Lett.*, 226:225–241, 2004.

A. M. Trehu, P. B. Flemings, N. L. Bangs, J. Chevalier, E. Gracia, J. E. Johnson, C.-S. Liu, X. Liu, M. Riedel, and M. E. Torres. Feeding methane vents and gas hydrate deposits at south Hydrate Ridge. *Geophys Res. Lett.*, 31:L23310, doi:10.1029/2004GL021286, 2004a.

A. M. Trehu, P. E. Long, M. E. Torres, G. Bohrmann, F. R. Rack, T. S. Collett, D. S. Goldberg, A. V. Milkov, M. Riedel, P. Schultheiss, N. L. Bangs, S. R. Barr, W. S. Borowski, G. E. Claypool, M. E. Delwiche, G. R. Dickens, E. Gracia, G. Guerin, M. Holland, J. E. Johnson, Y. J. Lee, C. S. Liu, X. Su, B. Teichert, H. Tomaru, M. Vanneste, M. Watanabe, and J. L. Weinberger. Three-dimensional distribution of gas hydrate beneath southern Hydrate Ridge: constraints from ODP Leg 204. *Earth Planet. Sci. Lett.*, 222:845–862, 2004b.

National Energy Technology Laboratory

626 Cochrans Mill Road
P.O. Box 10940
Pittsburgh, PA 15236-0940

3610 Collins Ferry Road
P.O. Box 880
Morgantown, WV 26507-0880

One West Third Street, Suite 1400
Tulsa, OK 74103-3519

1450 Queen Avenue SW
Albany, OR 97321-2198

2175 University Ave. South
Suite 201
Fairbanks, AK 99709

Visit the NETL website at:
www.netl.doe.gov

Customer Service:
1-800-553-7681